A Massive Star Is Born: How Feedback from Stellar Winds, Radiation Pressure, and Collimated Outflows Limits Accretion onto Massive Stars

Anna L. Rosen[1,2,3,4,5]

[1] Center for Astrophysics | Harvard & Smithsonian, 60 Garden Street, Cambridge, MA 02138, USA
[2] Center for Astronomy & Space Sciences, University of California, San Diego, La Jolla, CA 92093, USA; anna@ucsd.edu

Abstract

Massive protostars attain high luminosities as they are actively accreting and the radiation pressure exerted on the gas in the star's atmosphere may launch isotropic high-velocity winds. These winds will collide with the surrounding gas producing shock-heated ($T \sim 10^7$ K) tenuous gas that adiabatically expands and pushes on the dense gas that may otherwise be accreted. We present a suite of 3D radiation-magnetohydrodynamic simulations of the collapse of massive prestellar cores and include radiative feedback from the stellar and dust-reprocessed radiation fields, collimated outflows, and, for the first time, isotropic stellar winds to model how these processes affect the formation of massive stars. We find that winds are initially launched when the massive protostar is still accreting and its wind properties evolve as the protostar contracts to the main sequence. Wind feedback drives asymmetric adiabatic wind bubbles that have a bipolar morphology because the dense circumstellar material pinches the expansion of the hot shock-heated gas. We term this the "wind tunnel effect." If the core is magnetized, wind feedback is less efficient at driving adiabatic wind bubbles initially because magnetic tension delays their growth. We find that wind feedback eventually quenches accretion onto $\sim 30\,M_\odot$ protostars that form from the collapse of the isolated cores simulated here. Hence, our results suggest that $\gtrsim 30\,M_\odot$ stars likely require larger-scale dynamical inflows from their host cloud to overcome wind feedback. Additionally, we discuss the implications of observing adiabatic wind bubbles with Chandra while the massive protostars are still highly embedded.

Unified Astronomy Thesaurus concepts: Massive stars (732); Star formation (1569); Stellar feedback (1602); Stellar winds (1636); Stellar wind bubbles (1635)

1. Introduction

Massive stars ($\gtrsim 8\,M_\odot$) directly influence their environment with their intense radiation fields, fast stellar winds, and supernova explosions at the end of their short lives. The energy and momentum imparted to the interstellar medium (ISM) by these processes, known as stellar feedback, leads to inefficient star formation in giant molecular clouds (GMCs) and their host galaxies (Hopkins 2014; Gatto et al. 2017; Krumholz et al. 2019; Grudic et al. 2022). Stellar feedback has a direct consequence for the formation of massive stars because it can halt the accretion of material onto the star, thereby potentially affecting the maximum mass a star can achieve (Olivier et al. 2021).

Massive stars form from the gravitational collapse of dense ($\sim 10^4$–10^7 cm^{-3}), magnetized, turbulent, and cold (~ 10 K) molecular gas in GMCs (see reviews by Tan et al. 2014 and Rosen et al. 2020). Due to their short Kelvin–Helmholtz timescales, they achieve their main-sequence luminosities while they are actively accreting (Palla & Stahler 1991, 1992; Behrend & Maeder 2001; Hosokawa & Omukai 2009). Additionally, they produce powerful jets (hereafter collimated outflows) that are magnetically launched via the star–disk interaction (Shu et al. 1988; Pelletier & Pudritz 1992;

Kölligan & Kuiper 2018). Because of this, a common signature of massive star formation is the entrained molecular outflows that emanate from their birth sites when they are highly embedded and actively accreting (Maud et al. 2015; Rosen & Krumholz 2020; Avison et al. 2021). Significant theoretical attention has been given to the role that radiation pressure and collimated outflows play in massive star formation (e.g., Krumholz et al. 2009; Cunningham et al. 2011; Kuiper et al. 2015; Rosen et al. 2016; Kee & Kuiper 2019; Rosen et al. 2019; Rosen & Krumholz 2020). However, no attention has been given to the role that stellar winds (i.e., the stellar surface material that is launched due to the radiation pressure exerted on the gas in the star's atmosphere) might play during their formation. Since massive protostars attain high luminosities while they are actively accreting and contracting to the main sequence they should launch radiatively driven stellar winds when they are relatively cool ($T_{\rm eff} \gtrsim 15$ kK; Vink et al. 2001; Vink 2018). Therefore, stellar wind feedback may be important in regulating accretion onto massive protostars earlier, as compared to other modes of feedback, as they contract to the main sequence and are heavily embedded.

Stellar winds from main-sequence massive stars are roughly isotropic and leave the stellar surface at or above the escape speed of the star, which is $>10^3$ km s^{-1} for main-sequence massive stars (Leitherer et al. 1992; Vink et al. 2001). These fast winds collide with the surrounding ISM and thermalize, producing hot, shocked stellar wind material (Castor et al. 1975; Weaver et al. 1977; Koo & McKee 1992). Assuming all of the wind kinetic energy injected (where $\dot{E} = 1/2\dot{M}_{\rm w}v_{\rm w}^2$ is the rate of kinetic energy injected by winds, and $\dot{M}_{\rm w}$ and $v_{\rm w}$ are the

wind mass-loss rate and wind velocity) is thermalized the resulting temperature of the hot shock-heated gas should attain temperatures of (Rosen et al. 2021)

$$T_{X} \approx 10^{7} \left(\frac{v_{w}}{1000 \text{ km s}^{-1}} \right)^{2} \text{ K.} \qquad (1)$$

This hot gas will then cool via adiabatic expansion rather than significant radiative losses since cooling at these high temperatures is inefficient, resulting in energy-driven (i.e., energy-conserving) stellar wind feedback (Weaver et al. 1977; Koo & McKee 1992; Rosen et al. 2014, 2021). The resulting expansion will sweep up a dense shell of entrained molecular material, producing energy-driven adiabatic wind bubbles. However, at the shell interface a significant fraction of the kinetic energy from stellar winds can be lost via radiative cooling because the hot shock-heated gas and cold and turbulent interstellar gas can mix to form $T \sim 10^{4}$–10^{5} K gas that cools efficiently, thereby reducing the impact of wind feedback on larger scales (Rosen et al. 2014; Toala & Arthur 2018; Lancaster et al. 2021a, 2021b).

The hot gas produced by wind feedback emits thermal X-rays and therefore can be observed with X-ray telescopes like Chandra (Lopez et al. 2011; Rosen et al. 2014). Olivier et al. (2021) performed the first multiwavelength study of a large sample of galactic ultracompact and compact H II regions ($R_{Hii} \lesssim 0.5$ pc) that surround young massive stellar systems to determine the importance of different feedback mechanisms during their formation. They studied the hot $T \geqslant 10^{6}$–10^{7} K gas produced by stellar winds, the direct and dust-reprocessed radiation pressures, and the warm $T \approx 10^{4}$ K photoionized gas produced by photoionization. To study the importance of wind feedback they used Chandra archival data of 26 H II regions, of which only six had reliable detections ($\geqslant 10$ photons). Given that these H II regions were unresolved they were unable to separate the diffuse X-ray emission associated with the hot X-ray-emitting gas produced by wind feedback and the stellar sources that typically have hard $\gtrsim 3$ keV emission. Therefore, they were only able to determine upper limits for the hot gas pressures, P_{X}, in their sample. Regardless, they found that the majority of H II regions in their sample are dominated by the dust-reprocessed radiation pressure and they were unable to determine the importance of wind feedback. Therefore, it still remains uncertain how important wind feedback is during the early formation of massive stars.

Numerical simulations have shed light on the importance of wind feedback from massive stars in the context of star cluster formation. Dale et al. (2014) simulated the effect of photoionization and momentum-conserving wind feedback (i.e., they neglected the thermalization of stellar winds) from massive stars with self-consistent star formation and found that the momentum injected by winds was dynamically unimportant. However, they were likely underestimating the effect of wind feedback because they did not include the kinetic energy injected by stellar winds and therefore neglected the hot, thermalized gas that should be produced by the shock heating of stellar winds. Geen et al. (2021) simulated the effect of photoionizing radiation and wind feedback on GMC scales for main-sequence massive stars, including both the momentum and energy injection by winds, and found that the adiabatic wind bubbles that form are initially confined and grow to have complex asymmetric morphologies. Likewise,

Grudic et al. (2022) performed the first star cluster formation simulation with self-consistent individual star formation and protostellar evolution with feedback from collimated outflows, radiation pressure, photoionization, and stellar winds (including both momentum and energy injection), with the new STAR-FORGE framework (Grudic et al. 2021), to determine how these processes work in concert to quench star formation in GMCs. However, in their simulation stellar winds are only launched from massive stars once they reach the main sequence. They found that feedback from radiation and winds are responsible for quenching star formation in GMCs. While these simulations demonstrated the importance of wind feedback from massive stars they did not study the direct impact wind feedback has on the formation of individual massive protostars and the resulting wind bubbles that may form while they are actively accreting and contracting to the main sequence.

In this paper, we investigate these effects by performing 3D radiation-magnetohydrodynamics (RMHD) numerical simulations of the collapse of magnetized and unmagnetized turbulent massive prestellar cores into massive stellar systems, including both radiative and collimated outflow, and, for the first time, radiatively driven isotropic wind feedback to explore how both the energy and momentum injected by stellar winds affects massive star formation. This paper is organized as follows. We describe our numerical methodology and simulation design in Section 2. We present and discuss our results in Sections 3 and 4, respectively. Finally, we conclude and summarize our results in Section 5.

2. Numerical Method

In this paper, we simulate the formation of massive stars from the gravitational collapse of isolated magnetized and unmagnetized turbulent massive prestellar cores with the ORION2 adaptive mesh refinement (AMR) constrained-transport gravito-radiation-magnetohydrodynamics (RMHD) simulation code (Li et al. 2021). ORION2 includes MHD (Li et al. 2012), radiative transfer (Krumholz et al. 2007; Shestakov & Offner 2008; Rosen et al. 2017), self-gravity (Truelove et al. 1998), and Lagrangian accreting sink particles (Krumholz et al. 2004) that include a protostellar evolution model used to represent them as radiating (proto)stars (Offner et al. 2009). The star particles are coupled to subgrid prescriptions that model stellar feedback from both collimated protostellar outflows (Cunningham et al. 2011; Rosen et al. 2020) and isotropic radiatively driven stellar winds (Offner & Arce 2015; Rosen et al. 2021). We describe the equations solved by ORION2 and the boundary conditions for the simulations in Section 2.1, the simulation initial conditions in Section 2.2, our refinement and sink creation requirements in Section 2.3, and the stellar radiation, outflow, and wind feedback prescriptions in Section 2.4.

2.1. Evolution Equations and Boundary Conditions

The full gravito-RMHD equations solved by ORION2 that describe the dynamics of the fluid-sink (star) particle system for the simulations presented in this work are as follows:

$$\frac{\partial \rho}{\partial t} = -\nabla \cdot (\rho v) - \sum_{i} \dot{M}_{a,i} W_{a}(x - x_{i})$$
$$+ \sum_{i} \dot{M}_{o,i} W_{o,i}(x - x_{i})$$
$$+ \sum_{i} \dot{M}_{w,i} W_{w,i}(x - x_{i}), \qquad (2)$$

$$\frac{\partial(\rho \boldsymbol{v})}{\partial t} = -\boldsymbol{\nabla} \cdot (\rho \boldsymbol{v} \boldsymbol{v}) - \boldsymbol{\nabla}\left(P + \frac{B^2}{8\pi}\right) + \frac{1}{4\pi}\boldsymbol{B} \cdot \boldsymbol{\nabla} \boldsymbol{B}$$
$$- \rho \boldsymbol{\nabla}\phi - \lambda \boldsymbol{\nabla} E_{\rm R} - \sum_i \dot{\boldsymbol{p}}_{a,i}\, W_a(\boldsymbol{x} - \boldsymbol{x}_i)$$
$$+ \sum_i \dot{\boldsymbol{p}}_{\rm rad,i} + \sum_i \dot{\boldsymbol{p}}_{o,i}\, W_{o,i}(\boldsymbol{x} - \boldsymbol{x}_i)$$
$$+ \sum_i \dot{\boldsymbol{p}}_{w,i}\, W_{w,i}(\boldsymbol{x} - \boldsymbol{x}_i), \tag{3}$$

$$\frac{\partial(\rho e)}{\partial t} = -\boldsymbol{\nabla} \cdot \left[\left(\rho e + P + \frac{B^2}{8\pi}\right)\boldsymbol{v} - \frac{1}{4\pi}\boldsymbol{B}(\boldsymbol{v} \cdot \boldsymbol{B})\right]$$
$$- \rho \boldsymbol{v} \cdot \boldsymbol{\nabla}\phi - \kappa_{0P}\rho(4\pi B_P - cE_{\rm R})$$
$$+ \lambda\left(2\frac{\kappa_{0P}}{\kappa_{0R}} - 1\right)\boldsymbol{v} \cdot \boldsymbol{\nabla} E_{\rm R}$$
$$- \left(\frac{\rho}{m_{\rm p}}\right)^2 \Lambda(T_{\rm g}) - \sum_i \dot{\varepsilon}_{a,i} W_{a,i}(\boldsymbol{x} - \boldsymbol{x}_i)$$
$$+ \sum_i \dot{\varepsilon}_{\rm rad,i} + \sum_i \dot{\varepsilon}_{o,i} W_{o,i}(\boldsymbol{x} - \boldsymbol{x}_i)$$
$$+ \sum_i \dot{\varepsilon}_{w,i} W_w(\boldsymbol{x} - \boldsymbol{x}_i), \tag{4}$$

$$\frac{\partial E_{\rm R}}{\partial t} = \boldsymbol{\nabla} \cdot \left(\frac{c\lambda}{\kappa_{0R}\rho}\boldsymbol{\nabla} E_{\rm R}\right) + \kappa_{0P}\rho(4\pi B_P - cE_{\rm R})$$
$$- \lambda\left(2\frac{\kappa_{0P}}{\kappa_{0R}} - 1\right)\boldsymbol{v} \cdot \boldsymbol{\nabla} E_{\rm R} - \boldsymbol{\nabla} \cdot \left(\frac{3 - R_2}{2}\boldsymbol{v}E_{\rm R}\right)$$
$$+ \left(\frac{\rho}{m_{\rm p}}\right)^2 \Lambda(T_{\rm g}), \tag{5}$$

$$\frac{\partial \boldsymbol{B}}{\partial t} = \boldsymbol{\nabla} \times (\boldsymbol{v} \times \boldsymbol{B}), \tag{6}$$

$$\frac{dM_{\rm i}}{dt} = \dot{M}_{a,i} - \dot{M}_{o,i} - \dot{M}_{w,i}, \tag{7}$$

$$\frac{d\boldsymbol{x}_i}{dt} = \frac{\boldsymbol{p}_i}{M_{\rm i}}, \tag{8}$$

$$\frac{d\boldsymbol{p}_i}{dt} = -M_i\nabla\phi + \dot{\boldsymbol{p}}_{a,i}, \tag{9}$$

$$\nabla^2\phi = 4\pi G\left[\rho + \sum_i M_i\delta(\boldsymbol{x} - \boldsymbol{x}_i)\right]. \tag{10}$$

In these equations, ρ is the gas density, $\rho \boldsymbol{v}$ is the momentum density, ρe is the total internal plus kinetic gas energy density, $E_{\rm R}$ is the radiation energy density in the rest frame of the computational domain, $\boldsymbol{B}$ is the magnetic field, and ϕ is the gravitational potential. Equations (2)–(5) describe conservation of gas mass, gas momentum, gas total energy, and radiation total energy, respectively. They include terms describing the exchange of these quantities with the star particles (which are denoted by the subscript i), and exchange of energy and momenta between radiation, magnetic fields, gas, and star particles including contributions from stellar radiation, collimated protostellar outflows, and isotropic stellar winds. Equation (6) is the induction equation that describes the time evolution of the magnetic field in the ideal MHD limit, which assumes the magnetic field and fluid are well coupled. ORION2 uses a constrained-transport scheme that maintains $\boldsymbol{\nabla} \cdot \boldsymbol{B} = 0$ to machine accuracy (Li et al. 2012).

The gas follows an ideal equation of state so that the gas pressure is defined as

$$P = \frac{\rho k_{\rm B} T}{\mu m_{\rm H}} = (\gamma - 1)\rho e_{\rm T}, \tag{11}$$

where T is the gas temperature, μ is the mean molecular weight, γ is the ratio of specific heats, and $e_{\rm T}$ is the thermal energy of the gas per unit mass. We take $\mu = 2.33$, which is appropriate for molecular gas of solar composition (i.e., the initial prestellar core material composition), and $\gamma = 5/3$, which is appropriate for molecular gas at temperatures too low to excite the rotational levels of H_2 and the hot shock-heated gas produced by stellar wind feedback (Weaver et al. 1977; Rosen et al. 2016, 2021). Additionally, we assume the fluid is a mixture of dust and gas with a dust-to-gas mass ratio of 0.01 and assume the gas and dust temperatures are the same since, at the high densities modeled in this work, the dust will be thermally coupled to the gas (Hopkins et al. 2022).

ORION2 uses the (gray) flux limited diffusion (FLD) approximation to model the radiative emission and absorption by the gas and dust, which assumes that the radiative flux in the comoving frame is related to the gradient of the radiation energy density, to follow the evolution of the radiation field coupled to the fluid (see Krumholz et al. 2007 and Rosen et al. 2016 for more detail). The radiation-specific quantities in Equations (4)–(5) are the blackbody function $B_{\rm P} = ca_{\rm R}T^4/(4\pi)$, the density- and temperature-dependent Planck and Rosseland mean opacities, κ_{0P} and κ_{0R}, computed in the frame comoving with the gas, the (dimensionless) flux limiter λ, and the Eddington factor R_2 (Helling et al. 2000; Semenov et al. 2003; Krumholz et al. 2007). These last two quantities originate from the FLD approximation. Lastly, we include continuum and metal line cooling, which only become significant when $T \gtrsim 10^3$ K (i.e., when dust begins to sublime), with the cooling function $\Lambda(T)$, and we assume $\mu = 0.6$, which is appropriate for ionized gas of solar composition (Cunningham et al. 2011).

Equations (7)–(9) describe the dynamical evolution of the (proto)star particles, as indexed by the subscript i, which accrete nearby gas and interact with the fluid via gravity, stellar radiation, collimated protostellar outflows, and isotropic stellar winds. We describe the modeling of their feedback (i.e., the momentum and energy injected into the fluid) associated with their radiation fields, outflows, and winds in Section 2.4, but note here that the radiation-, outflows-, and wind-specific terms in Equations (2)–(4) affiliated with star particles are denoted with the rad, o, and w subscripts, respectively. The star particles are characterized by their mass M_i, position $\boldsymbol{x}_i$, momentum $\boldsymbol{p}_i$, angular momentum that describes the particle's spin axis $\boldsymbol{J}_i$, and luminosity ($\dot{\varepsilon}_{\rm rad,i}$), as determined by the protostellar evolution model described in Offner et al. (2009). They accrete mass, momentum, and energy from the computational grid via the weighting kernel $W_a(\boldsymbol{x} - \boldsymbol{x}_i)$, which is nonzero only within four radial cells of each particle following the sink particle accretion algorithm described in Krumholz et al. (2004), at rates $\dot{M}_{a,i}$, $\dot{\boldsymbol{p}}_{a,i}$, and $\dot{\varepsilon}_{a,i}$, respectively. The star particles' angular momentum and spin axis directions are updated via the subgrid model described in Fielding et al. (2015). Lastly, Equation (10) describes how the gravitational potential of the gas is advanced and includes contributions from the fluid and sink (star) particles.

Table 1
Physical Parameters and Simulation Outcomes for the Simulations Presented in This Work

Run		ROF$\mu_\phi\infty$	ROFW$\mu_\phi\infty$	ROFμ_ϕ2	ROFWμ_ϕ2	ROFμ_ϕ20	ROFWμ_ϕ20
Physical Parameter							
Mass-to-flux ratio	μ_ϕ	∞	∞	2	2	20	20
Magnetic field strength (mG)	B_z	0	0	0.81	0.81	0.081	0.081
Rad. feedback?		Yes	Yes	Yes	Yes	Yes	Yes
Outflows?		Yes	Yes	Yes	Yes	Yes	Yes
Winds?		No	Yes	No	Yes	No	Yes
Simulation Outcome							
Simulation end time ($t_{\rm ff}$)		1.05	0.91	1.39	1.05	0.92	0.85
Massive star mass ($M_\odot$)		35.76	30.25	34.00	31.89	28.75	27.58
Number of sinks		15	14	2	2	9	9
Star formation efficiency	$\frac{M_{\star,\,\rm tot}}{M_{\rm c}}$	0.32	0.24	0.23	0.21	0.25	0.23

Note. Each simulation begins with an isolated cold ($T_{\rm c} = 20$ K) dusty molecular magnetized or unmagnetized prestellar core with mass $M_{\rm c} = 150\,M_\odot$ and radius $R_{\rm c} = 0.1$ pc, corresponding to a surface density of $\Sigma = 1$ g cm^2. Each core is placed in a 0.4 pc box and is seeded with supersonic turbulence with an initial velocity dispersion of $\sigma_{\rm 1D} = 1.2$ km s^{-1}. Each simulation has a base grid of 128^3 cells and we allow for four levels of refinement, corresponding to a maximum resolution of 40 au.

The boundary conditions for the hydrodynamic, gravity, and radiation solvers are as follows. We impose outflow boundary conditions for the hydrodynamic update by setting the gradients of the hydrodynamic quantities (ρ, $\rho\mathbf{v}$, ρe) to be zero at the domain when advancing Equations (2)–(4) (Cunningham et al. 2011; Myers et al. 2013; Rosen et al. 2016, 2019) and set the gravitational potential, ϕ, to zero at all boundaries since the core boundaries are far removed from the domain boundaries when solving Equation (10). Finally, for each radiation update, we impose Marshak boundary conditions that bathe the simulation volume with a blackbody radiation field equal to $E_0 = 1.21 \times 10^{-9}$ erg cm^{-3}, corresponding to a 20 K blackbody, but allow for radiation generated within the simulation volume to escape freely (Krumholz et al. 2009; Cunningham et al. 2011; Myers et al. 2013; Rosen et al. 2016, 2019).

2.2. Initial Conditions

In this work, we perform six simulations of the collapse of turbulent, massive prestellar cores with feedback from stellar radiation, collimated outflows, and isotropic stellar winds to determine how these feedback mechanisms affect the formation and mass growth of massive stars. The first three simulations do not include isotropic stellar wind feedback (runs ROF$\mu_\phi\infty$, ROFμ_ϕ2, and ROFμ_ϕ20) and are only used to compare to identical simulations that do include wind feedback (runs ROFW$\mu_\phi\infty$, ROFWμ_ϕ2, and ROFWμ_ϕ20) to determine how wind feedback alters the accretion flow onto massive stars and affects the gas dynamics and gas structure near the star. In these simulations, the subgrid model for stellar winds is turned on when the star reaches an effective temperature of 12.5 kK following the wind mass-loss rate formulae from Vink et al. (2001) described in Section 2.4.3. Runs ROF$\mu_\phi\infty$ and ROFW$\mu_\phi\infty$ do not include magnetic fields whereas ROFμ_ϕ2 and ROFWμ_ϕ2 follow the collapse of magnetized cores. Likewise, runs ROFμ_ϕ20 and ROFWμ_ϕ20 follow the collapse of weakly magnetized cores and are used to compare with the results of the nonmagnetic and magnetic core collapse simulations in Section 3.8 since these simulations include a magnetic field strength much weaker than those observed in

dense molecular gas (Crutcher 2012; Hull & Zhang 2019). The initial conditions for the simulations described next are summarized in Table 1.

For all simulations presented here, we begin with an isolated prestellar core of molecular gas and dust (dust-to-gas ratio of 0.01) with mass $M_{\rm c} = 150\,M_\odot$ and radius $R_{\rm c} = 0.1$ pc corresponding to a surface density of $\Sigma = M_{\rm c}/\pi R_{\rm c}^2 = 1$ g cm^{-2} and mean density $\bar{\rho} = 2.4 \times 10^{-18}$ g cm^{-3} (1.2×10^6 H nuclei cm^{-3}) consistent with massive prestellar core densities and radii in extreme massive star-forming environments (e.g., Battersby et al. 2014; Ginsburg et al. 2015, 2018; Cao et al. 2019; Li et al. 2020). The corresponding characteristic freefall collapse timescale is $t_{\rm ff} \approx 42.8$ kyr. The core has a $\rho(r) \propto r^{-3/2}$ density profile, in agreement with observations of massive cores at the ~0.1 pc scale and clumps at the ~1 pc scale that find values of $\kappa_\rho = 1.5$–2 (e.g., Caselli & Myers 1995; Beuther et al. 2002; Mueller et al. 2002; Beuther et al. 2007; Zhang et al. 2009; Longmore et al. 2011; Butler & Tan 2012; Battersby et al. 2014; Stutz & Gould 2016; Beuther et al. 2021). The core's initial gas temperature is set to 20 K. Each core is placed in the center of the domain and the rest of the computational domain is filled with hot, diffuse gas with density $\rho_{\rm amb} = 0.01\rho_{\rm edge}$, where $\rho_{\rm edge}$ is the density at the edge of the core, and temperature $T_{\rm amb} = 2000$ K so that the core is in thermal pressure balance with the ambient medium. The opacity of the ambient medium is set to zero.

Runs ROFμ_ϕ2, ROFWμ_ϕ2, ROFμ_ϕ20, and ROFWμ_ϕ20 include magnetic fields to determine how magnetic pressure and magnetic tension affect the accretion of material onto massive (proto)stars and the development of wind-driven bubbles produced by their wind feedback (when winds are included). For runs ROFμ_ϕ2 and ROFWμ_ϕ2, the initial magnetic field is initially uniform in the z direction with $\mathbf{B} = B_0\hat{z}$, where $B_0 = 0.81$ mG, corresponding to a mass-to-flux ratio $\mu_\Phi = M_{\rm c}/M_\phi \simeq 2\pi G^{1/2}M_{\rm c}/\Phi = 2$, where $\Phi = \pi R_c^2 B_0$ is the magnetic flux through the core, consistent with observed values of $\Phi \simeq 2$–3 (Crutcher 2012). For runs ROFμ_ϕ20 and ROFWμ_ϕ20 we set $\mu_\Phi = 20$, yielding an initial weak magnetic field strength of $B_0 = 0.081$ mG. These weak-field magnetic runs are used for comparing the magnetic and nonmagnetic simulations.

Observed massive prestellar cores and clumps contain supersonic turbulence (e.g., see reviews by Hull & Zhang 2019

and Rosen et al. 2020). Following this, turbulent motions for the cores modeled here are included by seeding the initial gas velocities (v_x, v_y, and v_z) with a velocity power spectrum $P(k) \propto k^{-2}$, with modes between $k_{min} = 1$ to $k_{max} = 256$, as expected for supersonic turbulence (Padoan 1999; Boldyrev 2002; Cho & Lazarian 2003; Kowal et al. 2007). The turbulence mixture of gas is one-third compressive and two-thirds solenoidal, consistent with the natural mixture of a 3D fluid (Kowal et al. 2007; Kowal & Lazarian 2010). The onset of turbulence modifies the density and magnetic field distribution. All simulations are initialized with the same velocity perturbation power spectrum and a velocity dispersion of $\sigma_{1D} = 1.2$ km s^{-1}, corresponding to $\alpha_{vir} = 5\sigma_{1D}^2 R_c/GM_c = 1.1$ so that the core is roughly virialized (Bertoldi & McKee 1992). The turbulence will decay freely, however this simplification should have little effect on the results since the decay timescale, $\sim 2R_c/\sigma_{1D} \sim 0.16$ Myr (Goldreich & Sridhar 1995), is much longer than the run time for the simulations presented in this work.

We note that runs ROFμ_ϕ2, ROFWμ_ϕ2, ROFμ_ϕ20, and ROFWμ_ϕ20 also include magnetic pressure ($P_B = B^2/8\pi$), yielding $\alpha_{vir} = 5R_c/GM_c\left(\frac{1}{6}v_A^2 + \sigma_{1D}^2\right)$, where $v_A = B/\sqrt{4\pi\rho}$ is the Alfvén velocity. Therefore, the cores that include magnetic fields have slightly higher α_{vir} with values of 1.4 and 1.12 for the initial field strengths of $B_z = 0.81$ mG and $B_z = 0.081$ mG, respectively. As shown in Rosen & Krumholz (2020), this additional pressure term slows down the gravitational collapse of the prestellar core, resulting in lower accretion rates onto the massive star and broader entrained molecular outflows that are eventually ejected from the core because the core material is less bound.

2.3. Refinement and Sink Particle Creation Criteria

Each simulation has a base grid with volume $(0.4\,\text{pc})^3$ discretized by 128^3 cells and allows for four levels of refinement, resulting in a maximum resolution of 40 au. We note that the simulations presented in this work do not have the same maximum resolution of those presented in Rosen & Krumholz (2020), which had a maximum level of resolution of 20 au, corresponding to five levels of refinement. Refinement up to four AMR levels was chosen for the simulations presented in this work because the shock-heated gas ($T \sim 10^7$ K) produced by wind feedback (i.e., the thermalization of the wind kinetic energy) causes the time step to drop significantly since the Courant condition used to calculate the time step, which is a requirement for numerical stability, depends on the gas sound speed and velocities (Courant et al. 1967).

As the simulation evolves, the AMR algorithm automatically adds and removes finer grids. Cells are refined if they meet at least one of the following criteria: (1) any cell on level 0 (the base level) that has $\rho \geqslant \rho_{edge}$, so that the entire core is refined to level 1; (2) any cell where the density in the cell exceeds the Jeans density, given by

$$\rho_{max,J} = \frac{\pi J_{max}^2 c_s^2}{G\Delta x_l^2}\left(1 + \frac{0.74}{\beta^2}\right),\qquad(12)$$

where $c_s = \sqrt{kT/\mu m_p}$ is the isothermal sound speed, Δx_l is the cell size on level l, $\beta = 8\pi\rho c_s^2/B^2$ is the plasma parameter

(i.e., the ratio of the thermal gas pressure to the magnetic pressure)[6], and J_{max} is the maximum allowed number of Jeans lengths per cell, which is set to 1/8 following the MHD Truelove criterion (Myers et al. 2013); (3) any cell that is located within at least 16 cells of a sink particle; and (4) any cell within which the radiation energy density gradient exceeds $\nabla E_R > 0.15 E_R/\Delta x_l$.

Star particles form on the maximum AMR level when the Jeans condition for a Jeans number of $N_J = 0.25$ is exceeded following the resolution tests of Truelove et al. (1997). Star particles merge when they pass within one accretion radius of each other if the smaller particle has a mass less than $0.04\,M_\odot$, corresponding to the threshold for the largest plausible mass at which second collapse occurs for the protostar. Below this mass limit, a protostar represents a hydrostatic core that is several au in size and will likely be accreted by the more massive star (Masunaga & Miyama 1998; Masunaga & Inutsuka 2000). However, for masses above this value the protostar will have collapsed down to sizes of roughly several $R_\odot$, and therefore it is not appropriate to assume if the protostar will accrete onto the nearby (proto)star since the accretion radius for a sink particle is $4 \times \Delta x_4 = 160$ au.

2.4. Stellar Feedback Modeling

The simulations presented in this work follow the same stellar radiation and collimated outflow feedback modeling described in Rosen et al. (2016) and Rosen & Krumholz (2020), with the addition of radiatively driven isotropic wind feedback described in Rosen et al. (2021). Each star particle has a (direct) isotropic stellar radiation field and collimated outflows, which are launched at the poles along the star's angular momentum axis, that inject energy (ε) and momentum (p) into the surrounding fluid. Additionally, once the stellar effective temperature reaches $T_{eff} = 12.5$ kK the star is hot and luminous enough to produce an isotropic radiatively driven wind (Vink et al. 2001). We note that the outflows and winds are injected into the computational domain after the star accretes material and the resulting mass loss is subtracted from the stellar mass before the stellar radius and luminosity are updated by the protostellar evolution model. To trace the outflow and wind material we add two passively advected scalars to represent the outflow and wind gas that is injected, respectively. The modeling of these feedback processes are summarized next.

2.4.1. Stellar Radiation

The radiation pressure and radiative heating are modeled with the multifrequency hybrid adaptive ray-moment method (HARM^2) presented in Rosen et al. (2016) and Rosen et al. (2017), which treats both the direct (stellar) and indirect (dust-reprocessed) radiation fields. This method includes the direct solution of the frequency-dependent radiative transfer equation of the stellar radiation field along long characteristics (i.e., adaptive ray tracing) that are launched from the star isotropically and includes contributions from the stellar

---

6　In the limit that as $B \rightarrow 0$ we have that $\beta \rightarrow \infty$ and Equation (12) results to the classical Jeans limit (Truelove et al. 1997).

luminosity ($L_\star$) and accretion luminosity, given by

$$L_{\rm acc} = f_{\rm rad} \frac{GM_\star \dot{M}_\star}{R_\star}, \tag{13}$$

where $f_{\rm rad} = 3/4$ is the fraction of the gravitational potential energy of the accretion flow that is converted to radiation following Offner et al. (2009), $M_\star$ is the stellar mass, and $R_\star$ is the stellar radius determined by the subgrid protostellar evolution model. The accretion luminosity is modeled as a blackbody spectrum with temperature $T_{\rm acc} = (L_{\rm acc}/(4\pi R_\star^2 \sigma))^{1/4}$ such that $L_{\rm acc} = \int_0^\infty L_{{\rm acc},\nu} d\nu$. The rate of momentum and energy absorbed by the dusty fluid from the stellar radiation fields are given by $\dot{p}_{{\rm rad},i}$ and $\dot{\varepsilon}_{{\rm rad},i}$ in Equations (3) and (4), respectively. The frequency-dependent stellar spectra and dust opacities are taken from Lejeune et al. (1997) and Weingartner & Draine (2001) and are divided into 10 frequency bins (see Figure 1 of Rosen et al. 2016). The frequency range used for the stellar spectra, accretion spectra, and dust opacities is $1.87 \times 10^{12} - 3.29 \times 10^{16} \, s^{-1}$, which covers the far-IR (FIR) to extreme-UV (EUV) spectral range. Since dust is the primary absorber of the stellar radiation, dust absorption does not occur when the fluid temperature is $\geqslant 1500$ K, corresponding to the dust sublimation temperature. Instead the gas opacity is set to 0.01 cm^2 g, causing the warm gas carved out by feedback near the star to be effectively transparent to the stellar radiation field. This method is coupled to the gray FLD method described above to treat the (indirect) radiation field produced by thermal emission from dust (Krumholz et al. 2007; Rosen et al. 2016, 2017).

We note that our method is similar to the radiative transfer hybrid method developed by Mignon-Risse et al. (2020), which uses the gray M1 closure relation for stellar irradiation and gray FLD for the dust and gas. However, the HARM^2 multifrequency approach for stellar irradiation used in this work more accurately captures the momentum and energy injection from stellar irradiation because the dust opacity increases by several orders of magnitude across the FIR to EUV spectral range (e.g., see Figure 1 of Rosen et al. 2016).

2.4.2. Collimated Outflows

The magnetically launched collimated outflows are included as a subgrid model, first introduced by Cunningham et al. (2011) and updated by Rosen & Krumholz (2020) since proper modeling of the launching of outflows requires sufficiently high resolution and nonideal MHD processes (e.g., sub-au scales; see Kölligan & Kuiper 2018), which is prohibitively expensive for the simulations presented in this work. In this subgrid prescription, outflows are launched along the star's spin axis at the stellar poles, following the protostellar outflow model of Matzner & McKee (2000) that includes a collimation angle, θ_c, and launching fraction, $f_{\rm w}$, that is related to the accretion rate. For the simulations presented here, we take $\theta_c = 0.01$ and $f_o = 0.21$, which assumes that 21% of the accreted material is lost to outflows (i.e., $\dot{M}_{o,i} = f_o \dot{M}_{a,i}$). The outflows are injected in the eight nearest cells to the star (in

radius) with the weighting kernel $W_{o,i}(\boldsymbol{x} - \boldsymbol{x}_i)$ described in Cunningham et al. (2011).

The outflows are launched at a fraction $f_k = 0.3$ of the Keplerian velocity, such that the outflow velocity is $v_0 = f_k \sqrt{GM_\star/R_\star}$. The outflows inject mass $\dot{M}_o$, momentum $\dot{p}_o = \dot{M}_0 v_o$, kinetic energy $\dot{E}_{k,o} = \frac{1}{2} \dot{M}_o v_o^2$, and thermal energy $\dot{E}_{T,o} = \frac{\dot{M}_o k T_o}{\mu_o m_H (\gamma - 1)}$, where T_o is the outflow gas temperature taken to be the star's effective temperature when $T_{\rm eff} < 10^4$ K and $T_o = 10^4$ K otherwise and $\mu_o = 1.27$. The values used in these simulations for f_o and v_o are chosen to match the observed outflow momentum, $0.01 \lesssim f_o v_o \lesssim 0.15$, in low- and high-mass star-forming regions (Cunningham et al. 2011). In agreement, Rosen & Krumholz (2020) found that these outflow properties agree well with the energetics from entrained molecular outflows observed in high-mass star-forming regions (Maud et al. 2015).

2.4.3. Isotropic Stellar Winds

In runs ROFW$\mu_\phi \infty$, ROFW$\mu_\phi 2$, and ROFW$\mu_\phi 20$, the star produces an isotropic stellar wind that is launched by the star's radiation pressure (i.e., a radiatively driven wind) when the star's effective temperature is $T_{\rm eff} \geqslant 12{,}500$ K following the mass-loss rate analytic formulae developed by Vink et al. (2001). As shown in Figure 12 and described in Section 3.4, wind launching typically starts when the contracting protostar in the simulations presented here reaches $\sim 20 \, M_\odot$. The wind mass-loss rate formulae used in these simulations, which depend on the stellar properties, are adapted from Monte Carlo simulations that follow the fate of a large number of photons from below the stellar photosphere that calculates the radiative acceleration (i.e., launching) of wind material from the stellar surface. Vink et al. (2001) show that the wind mass-loss rates experience a jump around $T_{\rm eff} \approx 25{,}000$ K, known as the bistability jump, due to a change in the ionization state in the lower stellar photosphere (i.e., Fe IV recombines to form Fe III) leading to Fe ions that are more efficient line drivers on the hot side of the bistability jump. On the hot side of the bistability jump the mass-loss rate decreases by a factor of ~ 5 but the wind velocity, v_∞, increases by a factor of 2.

Assuming solar metallicity, the wind mass-loss rate for the cool side of the bistability jump is

$$
\begin{aligned}
\log_{10}(\dot{M}_\star) = {} & -6.688 + 2.210 \log_{10}\left(\frac{L_\star}{10^5 \, L_\odot}\right) \\
& - 1.339 \log_{10}\left(\frac{M_\star}{30 \, M_\odot}\right) \\
& - 1.601 \log_{10}\left(\frac{v_\infty/v_{\rm esc}}{2.0}\right) \\
& + 1.07 \log_{10}\left(\frac{T_{\rm eff}}{20 \, {\rm kK}}\right),
\end{aligned}
\tag{14}
$$

where $v_{\rm esc} = \sqrt{2GM_\star/R_\star}$ is the escape speed at the star's surface. On the hot side of the bistability jump the wind
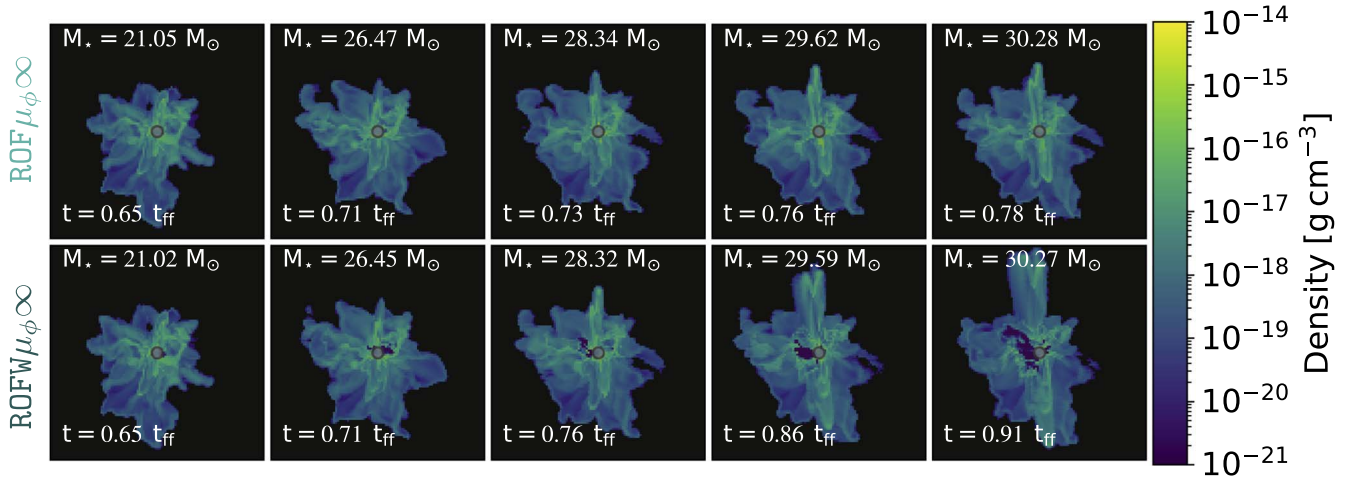
Figure 1. Density slices for runs ROF$\mu_\phi\infty$ (top row) and ROFW$\mu_\phi\infty$ (bottom row) as a function of primary stellar mass. The most massive star (denoted by the gray circle) is located at the center of each panel and the slice is oriented such that its angular momentum axis points up, in order to highlight the density structure of the outflows. The primary stellar mass and the simulation time, in units of $t_{\rm ff}$, are shown in the top-left and bottom-left corners of each panel, respectively. Each panel is $(0.4 \text{ pc})^2$.

mass-loss rate becomes

$$\log_{10}(\dot{M}_\star) = -6.697 + 2.194 \log_{10}\left(\frac{L_\star}{10^5 L_\odot}\right)$$
$$- 1.313 \log_{10}\left(\frac{M_\star}{30 M_\odot}\right)$$
$$- 1.226 \log_{10}\left(\frac{v_\infty/v_{\rm esc}}{2.0}\right)$$
$$+ 0.933 \log_{10}\left(\frac{T_{\rm eff}}{40 \text{ kK}}\right)$$
$$- 10.92 \left(\log_{10}\left(\frac{T_{\rm eff}}{40 \text{ kK}}\right)\right)^2. \qquad (15)$$

To determine which mass-loss recipe to use we first compute the bistability jump temperature following Equation (15) from Vink et al. (2001). If the (proto)star is on the cool (hot) side of the bistability the wind velocity (v_∞) is taken to be 1.3 $v_{\rm esc}$ (2.6 $v_{\rm esc}$) following values of $v_\infty/v_{\rm esc}$ determined by both theory and observations of winds from B and O stars (Vink et al. 2001, and references therein).

The winds are injected in a sphere encompassing the eight nearest cells to the star in radius ($R_{\rm w,inj} = 320$ au) with the weighting kernel $W_{w,i}(\boldsymbol{x} - \boldsymbol{x}_i)$ where each cell has an equal weight so that the total mass, momentum, and kinetic and thermal energies injected within this region are $\dot{M}_w$, $\dot{p}_w = \dot{M}_w v_\infty$, $\dot{E}_{k,w} = \frac{1}{2}\dot{M}_w v_\infty^2$, and $\dot{E}_{T,w} = \frac{\dot{M}_w k T_w}{\mu_o m_H(\gamma - 1)}$, respectively. We take $T_w = 10^4$ K and $\mu_o = 1.27$.

Pittard et al. (2021) found that in order to resolve the wind-bubble dynamics accurately the wind injection radius, $R_{\rm w,inj}$, must be smaller than a characteristic injection radius given by

$$R_{\rm max,inj} = \left(\frac{\dot{M}_w v_w}{4\pi P_{\rm amb}}\right)^{1/2}, \qquad (16)$$

where $P_{\rm amb}$ is the total ambient pressure including the thermal, turbulent, and magnetic pressures. They find that the wind-bubble momentum is within 25% of the true value if $\chi_w \equiv R_{\rm w,inj}/R_{\rm max,inj} \leqslant 0.1$. As will be shown in Figure 12, the

initial wind properties are $\dot{M}_w \sim 10^{-7} \, M_\odot \, {\rm yr}^{-1}$ and $v_w \sim 500$ km s^{-1}. For the core properties simulated in this work we find that our wind injection region is properly resolved with χ_w values of 0.062, 0.076, and 0.063 for runs ROFW$\mu_\phi\infty$, ROFW$\mu_\phi 2$, and ROFW$\mu_\phi 20$, respectively.

3. Results

3.1. Density Structure

Figure 1 shows density slice snapshots for runs ROF$\mu_\phi\infty$ (top row) and ROFW$\mu_\phi\infty$ (bottom row) at similar primary (most massive) stellar mass. Each panel covers the full domain to show the density structure of the entire core and the entrained molecular outflows that are powered by the protostellar collimated outflows, which are eventually ejected from the core (see, e.g., Rosen & Krumholz 2020). We only include snapshots for each run when the primary star is hot enough to launch winds (i.e., when $T_{\rm eff} \gtrsim 12.5$ kK, corresponding to when $M_\star \gtrsim 21 \, M_\odot$) to follow how wind feedback alters the density structure of gas near the primary star. Comparison of these snapshots for runs ROF$\mu_\phi\infty$ (top row) and ROFW$\mu_\phi\infty$ (bottom row) show that inclusion of wind feedback leads to low-density regions near the star that are not spherical even though the winds are launched isotropically.

As we show in Section 3.2, this low-density gas is produced by the shock heating of the fast-flowing stellar wind material (see, e.g., Section 2 of Rosen et al. 2021) that then undergoes adiabatic expansion (i.e., $P\,dV$ work) and carves out regions of low-density hot tenuous gas near the star. Since the density distribution near the primary star is turbulent with varying density, the asymmetry of the wind-driven "bubble" demonstrates that the low-density gas produced by stellar wind feedback follows the path of least resistance (i.e., undergoes greater expansion in regions of lower density), thereby carving out a nonspherical structure near the star that grows in time as the winds are continuously injected.

Comparison of runs ROF$\mu_\phi\infty$ and ROFW$\mu_\phi\infty$ shows that inclusion of wind feedback slows down the mass growth of the primary star. Hence, the entrained outflows that are ejected from the core are larger and more pronounced by the end of run ROFW$\mu_\phi\infty$ as compared to run ROF$\mu_\phi\infty$ at the same primary
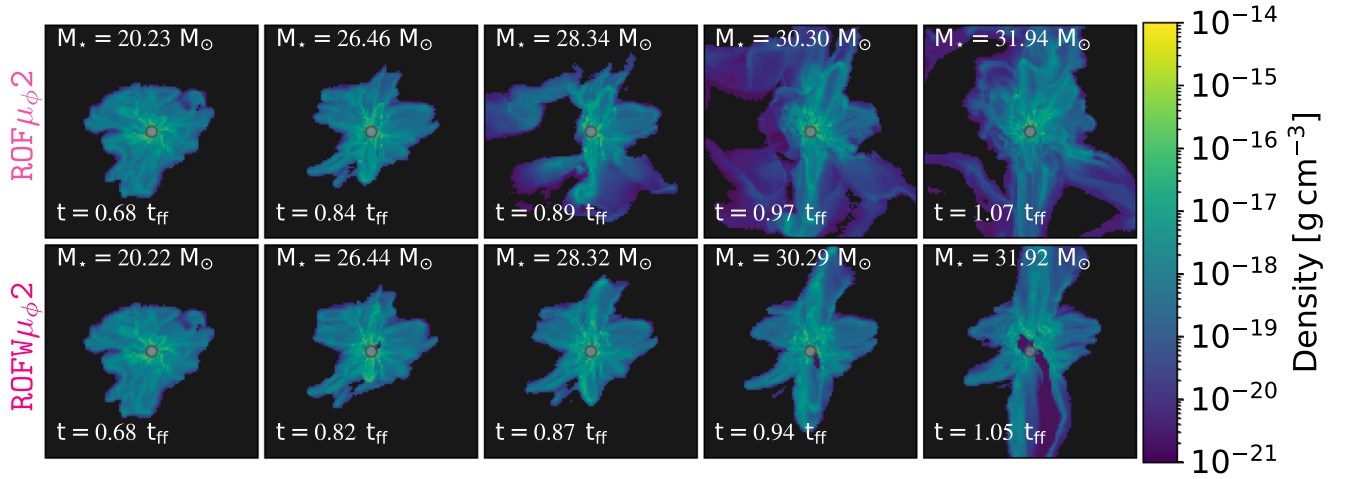
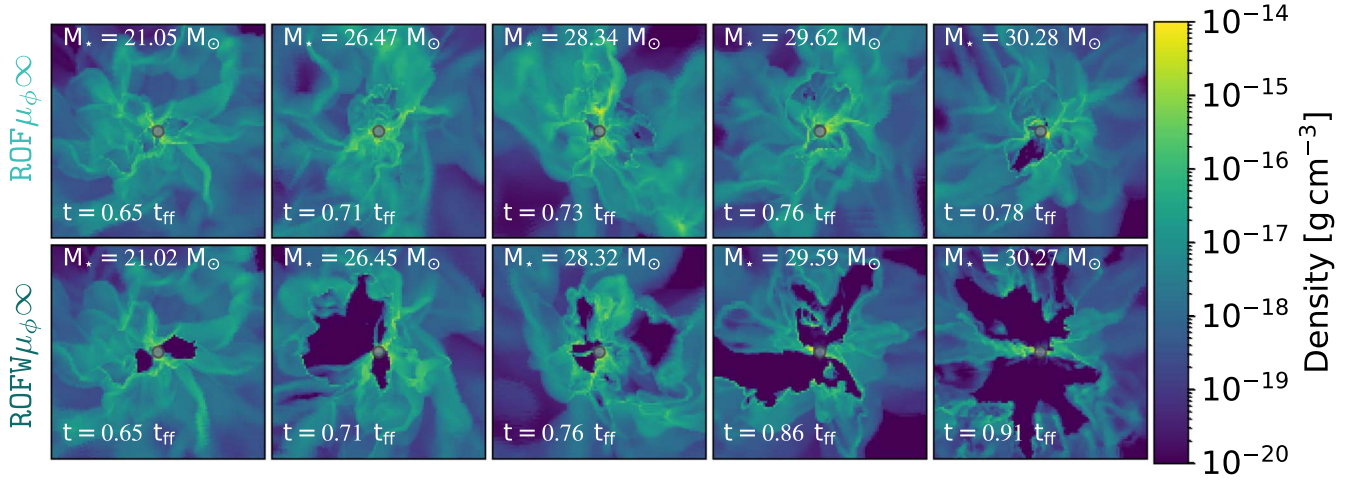**Figure 2.** Same as Figure 1 except now for runs ROFμ_ϕ2 (top row) and ROFWμ_ϕ2 (bottom row).

Figure 3. Zoom-in density slices for runs ROF$\mu_\phi\infty$ (top row) and ROFW$\mu_\phi\infty$ (bottom row) as a function of primary stellar mass. The most massive star is located at the center of each panel as marked by the gray circle. Each slice is oriented such that the mass-weighted angular momentum axis of the gas within a radius of 500 au from the primary star points up in order to highlight the wind-driven bubbles that are perpendicular to the dense circumstellar gas. The primary stellar mass and the simulation time are shown in the top-left and bottom-left corners of each panel, respectively. Each panel is $(0.1 \text{ pc})^2$.

stellar mass because the outflows are injected for a longer period of time. Therefore, these results suggest that, in the absence of magnetic fields, wind feedback eventually reduces the accretion rate onto massive stars once the star has strong winds because the kinetic energy injected by stellar winds is thermalized near the star and generates hot, low-density gas that adiabatically expands, pushing high-density material away that may otherwise be accreted onto the star. We describe the evolving wind properties in detail in Section 3.5.

This picture changes when magnetic fields are included. Figure 2 shows snapshots of the density slices for runs ROFμ_ϕ2 (top row) and ROFWμ_ϕ2 (bottom row) at the same primary stellar mass. In run ROFWμ_ϕ2 winds are launched when the star reaches $\sim 20\,M_\odot$, which is slightly less than the primary stellar mass in run ROFW$\mu_\phi\infty$. This difference is due to the different accretion history of the primary star, which affects the radial evolution of the protostar and is described in more detail in Section 3.4. Comparison of runs ROFWμ_ϕ2 and ROFW$\mu_\phi\infty$ in the bottom rows of Figures 1 and 2 show that wind feedback is less effective at producing expanding adiabatic wind bubbles when the surrounding material is magnetized. For example, in run ROFW$\mu_\phi\infty$ wind feedback produces a small wind-driven bubble almost immediately once winds are launched, but when

the core is magnetized wind feedback does not produce the hot shock-heated, low-density gas until the star reaches $\sim 30\,M_\odot$. Furthermore, the last panel of the bottom row in Figure 2 shows that the hot gas vents through the low-density gas carved out by protostellar outflows in the bottom outflow lobe, thereby suggesting that the hot, low-density gas produced by wind feedback more readily expands in the low-density regions carved out by protostellar outflows. This is explored in more detail in Section 3.7.

Comparison of runs ROFμ_ϕ2 and ROFWμ_ϕ2 suggests that the growth rate of the massive star does not change significantly when feedback from stellar winds are included if the core is magnetized, and is described in more detail in Section 3.8. Regardless, these simulations demonstrate that feedback from stellar winds eventually produces localized low-density non-spherical cavities near the star that expand whereas protostellar outflows lead to larger-scale collimated entrained molecular outflows that are eventually ejected from the core.
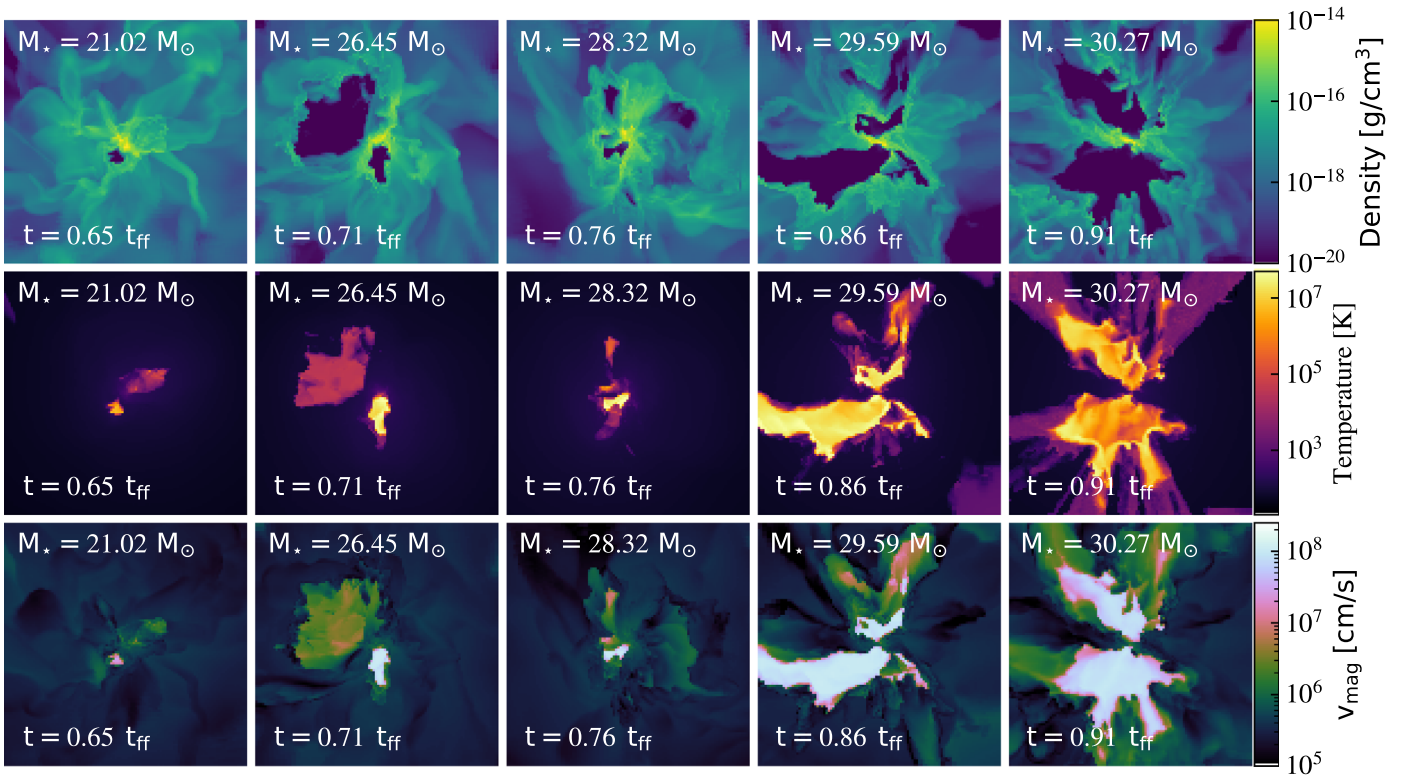
3.2. Wind-driven Bubble Morphology

Figures 3 and 4 show zoom-ins of the density slices presented in Figures 1 and 2, respectively, except now each slice is oriented
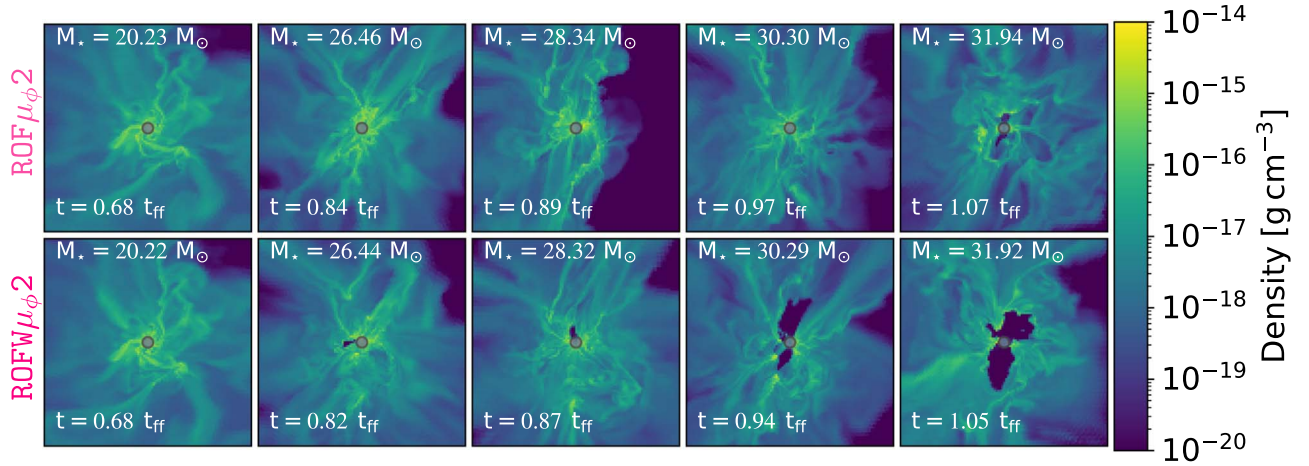
Figure 4. Same as Figure 3 except now for runs ROFμ_ϕ2 (top row) and ROFWμ_ϕ2 (bottom row).

Figure 5. Zoom-in thin-density (top row), temperature (middle row), and velocity (bottom row) projections for run ROFW$\mu_\phi\infty$ as a function of primary stellar mass. The most massive star is located at the center of each panel and is marked by the gray circle. Each projection is oriented such that the mass-weighted angular momentum axis of the gas within a radius of 500 au from the primary star points up in order to highlight the wind-driven bubbles. Each panel is $(0.1\ \mathrm{pc})^2$.

such that the mass-weighted angular momentum axis of the gas near the massive star points up. This orientation is chosen to highlight the morphology of the low-density wind-driven bubbles or lobes that are launched perpendicular to the star's equatorial plane, because along this direction the circumstellar gas is densest due to the conservation of angular momentum from the infalling core material, which is described in more detail in Section 4. Comparison of runs ROFW$\mu_\phi\infty$ and ROFWμ_ϕ2 (bottom rows) with the simulations that do not include wind feedback (runs ROF$\mu_\phi\infty$ and ROFμ_ϕ2; top rows) in Figures 3 and 4 demonstrates that the low-density bubbles produced near the primary star are due to wind feedback and not due to radiation pressure. The snapshots for the simulations that do not include

wind feedback show that radiation pressure only begins to drive low-density radiation-pressure-dominated bubbles near the star when it reaches $\sim 30\,M_\odot$ for run ROF$\mu_\phi\infty$ and $\sim 32\,M_\odot$ for run ROFμ_ϕ2. Hence, our results suggest that wind feedback drives low-density cavities before radiation pressure becomes strong enough to produce radiation-pressure-dominated bubbles.

These pinched low-density wind bubbles are produced by the shock heating (i.e., thermalization) of the wind material, as shown in Figures 5 and 6 for runs ROFW$\mu_\phi\infty$ and ROFWμ_ϕ2, respectively. These figures show zoom-ins of the thin mass-weighted projections of the gas density (top panels), gas temperature (middle panels), and gas velocity magnitude (bottom panels). We find that the shock-heated gas reaches
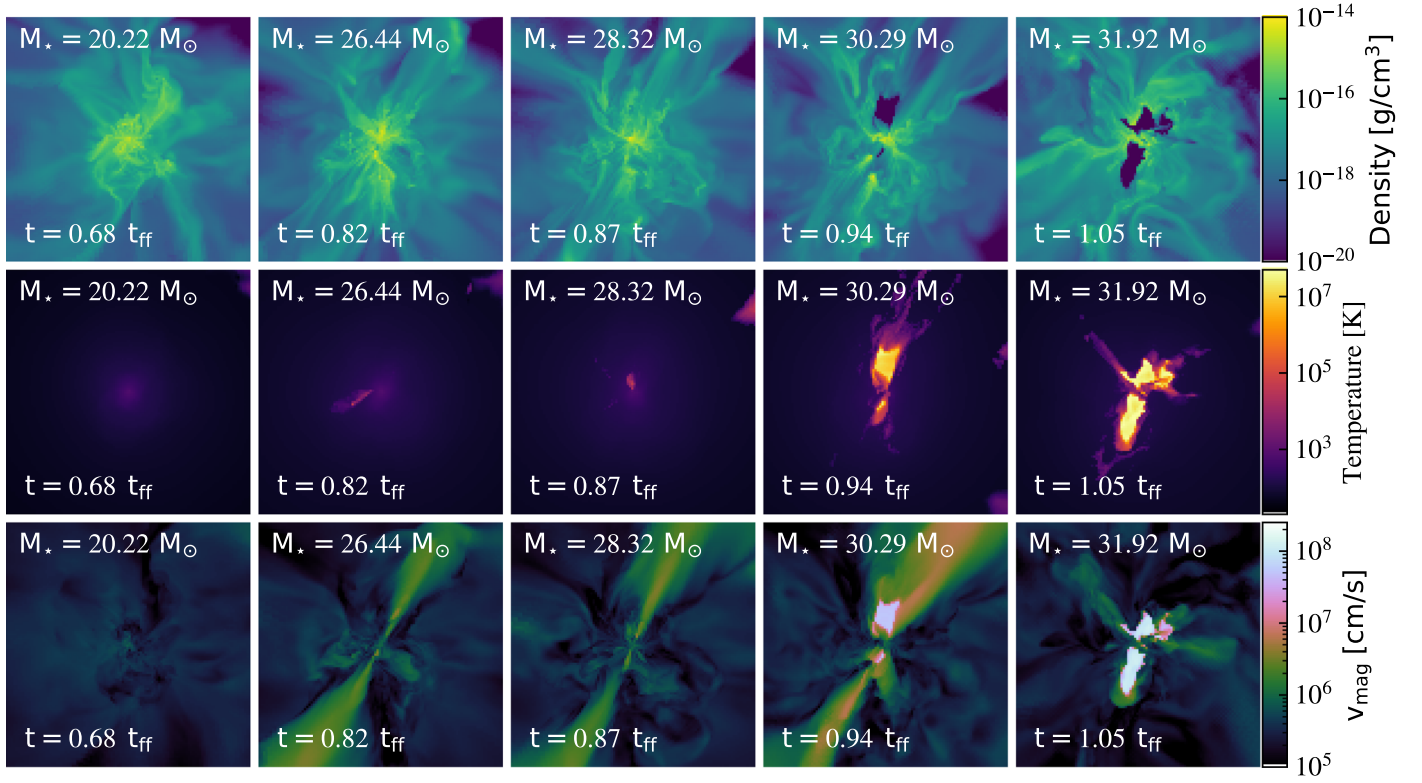
Figure 6. Same as Figure 5 except now for run ROFWμ$_\phi$2.

temperatures of $T \sim$ few $\times$ 10^6–10^7 K, corresponding to $c_s \sim 100$–400 km s^{-1}, that adiabatically expands. However, the majority of the wind-bubble volume contains free-flowing wind material with velocities $\sim10^3$ km s^{-1} that has yet to be thermalized, but the velocities reach the expected shock-heated velocities near the dense shell interfaces. For run ROFWμ$_\phi\infty$ we find that the wind-driven lobes can be crushed by the surrounding dense and infalling material. Eventually, as seen in the last panels of Figure 5, the winds become powerful enough to produce sustained wind-driven lobes.

Comparison of Figures 5 and 6 show that the wind-driven bubbles are larger for the unmagnetized core and by the end of both runs the asymmetric lobes extend above and below the massive star. The wind-driven lobes by the end of run ROFWμ$_\phi$2 are smaller in size because they are confined by the magnetic tension in the surrounding dense gas, which is explored in more detail in Section 3.8. This confining effect was also found for the radiation-pressure-dominated bubbles presented in Rosen & Krumholz (2020).

3.3. Accretion Disk Formation and Evolution

Figure 7 shows thin-density projections of the dense circumstellar material that surrounds the primary star along its equatorial plane for runs ROFμ$_\phi\infty$ (top row) and ROFWμ$_\phi\infty$ (bottom row) at similar primary stellar mass. Eventually, a high-density circumstellar accretion disk (i.e., a resolved accretion disk with a radius larger than the 160 au accretion zone radius of the sink particle) forms at late times for both runs because the accretion disk structure depends on the angular momentum content of the collapsing core, which is larger for material that is farther out. Given that run ROFWμ$_\phi\infty$ ran for a longer time the accretion disk is larger and more pronounced when the star reaches $\sim29\,M_\odot$ (i.e., the

last two panels in the bottom row) as compared to run ROFμ$_\phi\infty$ at the same primary stellar mass.

Comparison with the bottom row of Figure 3 shows that the presence of this high-density accretion disk causes the hot shock-heated gas produced by wind feedback to expand more freely along the polar directions of the primary star where the gas density is lower. This effect is the most pronounced for the last two snapshots in Figure 3, confirming that the dense accretion disk quenches the destructive effect of wind feedback near the star along the plane of the accretion disk.

In contrast, the influence of magnetic fields reduces disk formation due to magnetic braking, as shown in Figure 8, which shows thin-density projections of the dense circumstellar material, as a function of primary stellar mass, that surround the primary star along its equatorial plane for runs ROFμ$_\phi$2 (top row) and ROFWμ$_\phi$2 (bottom row). Rosen & Krumholz (2020) showed that magnetic braking, which removes angular momentum from the infalling material as the core collapses inhibits the formation of a discernible accretion disk around the massive star; however, higher-resolution and/or nonideal MHD effects such as ambipolar diffusion and ohmic resistivity may reduce how much angular momentum is removed, leading to smaller accretion disks than those produced when magnetic fields are not included (e.g., Seifried et al. 2012; Myers et al. 2013; Zhao et al. 2020; Commerçon et al. 2021; Mignon-Risse et al. 2021). Such effects are not explored in this work. Regardless, the bottom row of Figure 8 demonstrates that a noticeable accretion disk does not form around the primary star but the material near the primary star achieves high densities ($\rho \sim 10^{-15}$ g cm^{-3}), which inhibits wind-bubble expansion leading to the bipolar morphology of the wind bubble.

Eventually, as seen in the last two panels in the bottom row of Figure 8, feedback from winds does blow away material near
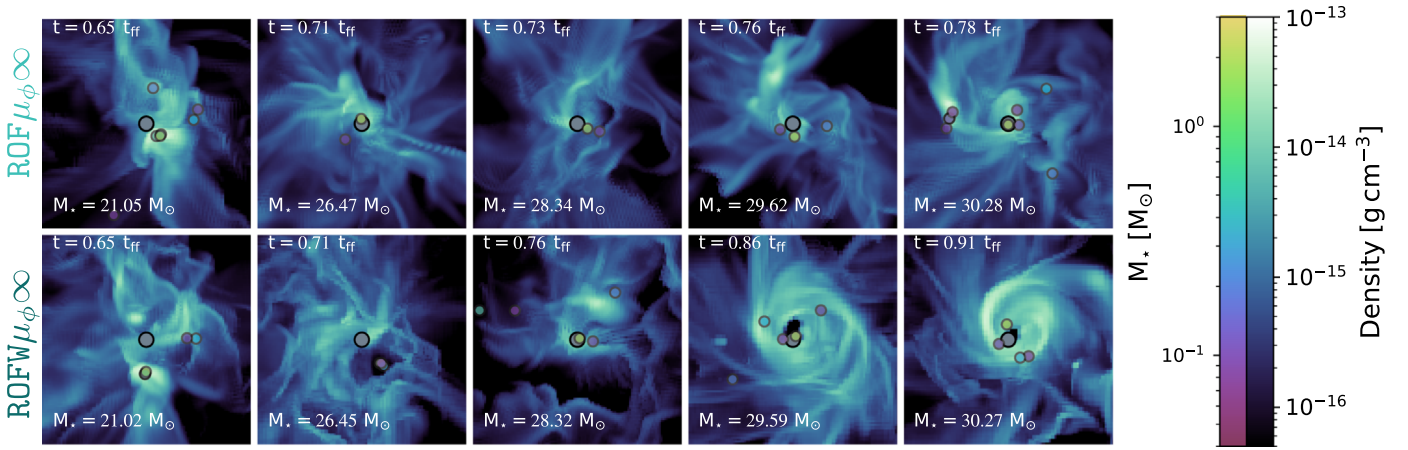
Figure 7. Density-weighted density thin projections for runs ROF$\mu_\phi\infty$ (top row) and ROFW$\mu_\phi\infty$ (bottom row) shown at similar primary stellar masses. The projections have been oriented so that the angular momentum axis of the material within 500 au of the primary star points out of the page, in order to highlight the accretion disk. In each panel, the most massive star is at the center (gray circle) and companion stars with masses greater than 0.04 $M_\odot$ are overplotted on all panels. The color of the star indicates its mass, as shown in the color bar. Each panel is (3000 au)^2 in area, and the projection is taken over a depth of 500 au in front of and behind the massive star.
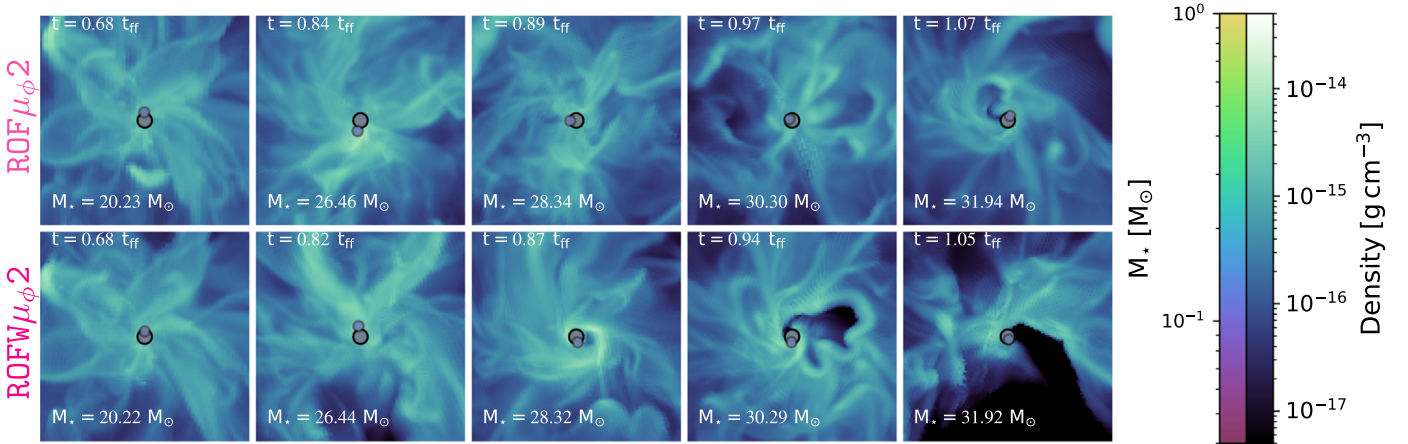
Figure 8. Same as Figure 7 except now for runs ROFμ_ϕ2 (top row) and ROFWμ_ϕ2 (bottom row).

the star along the equatorial plane. However, when comparing to the last two panels of the bottom row of Figure 4, the hot gas is beamed along directions perpendicular to the dense circumstellar gas producing wind-driven lobes above and below the star. These lobes are less pronounced than those produced in run ROFW$\mu_\phi\infty$. This effect is likely due to accumulation of dense material along the equatorial plane near the star and the magnetic tension along the wind-driven lobe edges, which we explore in Section 3.8.

3.4. Massive Protostar Properties

The physical properties of the massive (primary) protostar as a function of simulation time for runs ROF$\mu_\phi\infty$, ROFμ_ϕ2, ROFW$\mu_\phi\infty$, and ROFWμ_ϕ2 are shown in Figure 9. The left-hand column shows the accretion rate (top panel) and stellar mass (bottom panel). When magnetic fields are not included winds reduce the mass growth of the primary star: the accretion rate eventually drops when wind feedback becomes important and the mass growth of the massive star decreases appreciably when the star reaches $M_\star \sim 27\,M_\odot$. Comparing these panels with the gas properties near the star in Figure 5 shows that this drop in the accretion rate is due to the development and subsequent growth of

the wind-driven bubbles, thereby eventually quenching the accretion flow. The mass growth eventually plateaus, suggesting that stellar winds may be responsible for halting accretion onto massive stars.

Runs ROFμ_ϕ2 and ROFWμ_ϕ2 show a different scenario. If the protostellar core is magnetized, the accretion rate actually increases for run ROFWμ_ϕ2 once winds are launched by the star, causing the mass growth of the massive star to increase slightly as compared to run ROFμ_ϕ2. However, this increase is temporary because once the star reaches $\sim 30\,M_\odot$ wind feedback begins to produce hot shock-heated gas near the star that gradually expands, as shown in the last two columns in Figure 6. As will be shown in the next subsection, this behavior occurs when the protostar crosses the bistability jump, described in Section 2.4.3, where its wind velocity increases by a factor of ~ 2. This increase in velocity will reduce radiative losses for the shock-heated gas during the free-expansion stage of the wind bubble (i.e., the "fast winds" scenario by Koo & McKee 1992) thereby making wind feedback more effective. Hence, when winds are initially launched the magnetized material near the primary star delays the effect of wind feedback in reducing the accretion flow but this is short lived and eventually, at a greater stellar mass than
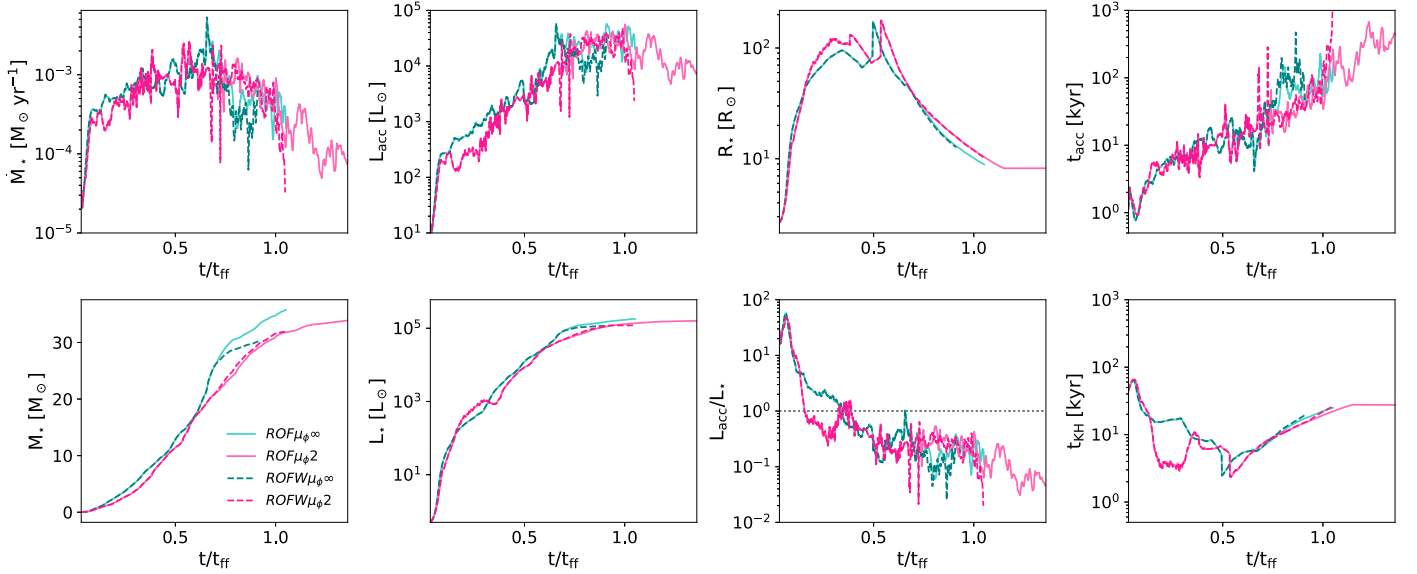
Figure 9. Primary protostar properties as a function of simulation time for runs ROF$\mu_\phi \infty$ (light teal solid lines), ROFW$\mu_\phi \infty$ (teal dashed lines), ROF$\mu_\phi 2$ (light pink solid lines), and ROFW$\mu_\phi 2$ (dark pink dashed lines). The top row shows the primary star's accretion rate (left panel), accretion luminosity (middle-left panel), radius (middle-right panel), and accretion timescale $t_{acc} = M_\star / \dot{M}_\star$ (right panel). The bottom row shows the primary star's mass (left panel), internal (stellar) luminosity (middle-left panel), the ratio of the accretion to internal luminosity (middle-right panel), and Kelvin–Helmholtz timescale $t_{KH} = GM_\star^2 / R_\star L_\star$ (right panel). The gray dashed line in the bottom middle-right panel denotes where this $L_{acc}/L_\star$ is equal to 1.
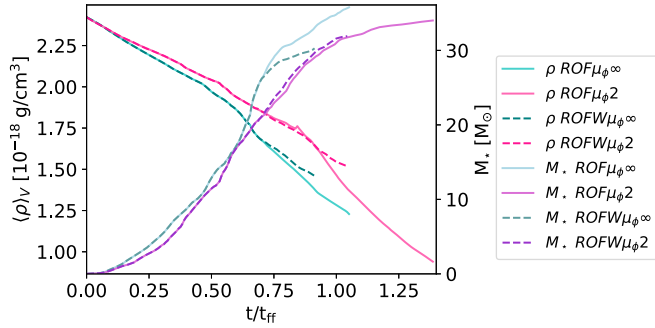
Figure 10. Volume-weighted average density within a sphere of 0.1 pc (i.e., the initial core radius) as a function of simulation time (left panel) for runs ROF$\mu_\phi \infty$ (light teal solid line), ROFW$\mu_\phi \infty$ (teal dashed line), ROF$\mu_\phi 2$ (light pink solid line), and ROFW$\mu_\phi 2$ (dark pink dashed line). The left panel also shows the evolution of the primary stellar mass (left y-axis) for runs ROF$\mu_\phi \infty$ (light blue solid line), ROFW$\mu_\phi \infty$ (dark blue dashed line), ROF$\mu_\phi 2$ (light purple solid line), and ROFW$\mu_\phi 2$ (purple dashed line).

seen in run ROFW$\mu_\phi \infty$ ($\sim 31\,M_\odot$ versus $\sim 27\,M_\odot$), wind feedback reduces accretion onto the massive star. This is discussed in more detail in Section 3.8.

The decrease (increase) in the accretion rate for run ROFW$\mu_\phi \infty$ (ROFW$\mu_\phi 2$) can be quantified by comparing the evolution of the volume-weighted mean density to the stellar mass growth as shown in Figure 10. This figure shows the volume-weighted core density, including contributions from both the outflow and wind material (note that these quantities are low compared to the nonaccreted core material), within a sphere of 0.1 pc (i.e., the initial core radius) as a function of simulation time for runs ROF$\mu_\phi \infty$, ROF$\mu_\phi 2$, ROFW$\mu_\phi 2$, and ROFW$\mu_\phi \infty$. The evolution of the massive star's mass is overplotted. As the massive star grows in mass the average density decreases for all runs. This decrease is greater for runs without magnetic fields because the massive stars have a faster growth rate. The average density slightly increases for runs ROFW$\mu_\phi \infty$ and ROFW$\mu_\phi 2$ as compared to runs ROF$\mu_\phi \infty$ and

ROF$\mu_\phi 2$ when the mass growth for the massive stars plateau because wind feedback becomes important. This slight increase occurs earlier for run ROFW$\mu_\phi \infty$ as compared to run ROFW$\mu_\phi 2$ because the accretion rate drops earlier due to the formation and expansion of the wind-driven bubbles.

The top-left middle panel, bottom-left middle panel, and bottom-right middle panel of Figure 9 show the primary star's accretion luminosity given by Equation (13), internal (stellar) luminosity, and the ratio of these two quantities as a function of simulation time. When the star is less than several $M_\odot$ the accretion luminosity is larger than the stellar luminosity, but eventually the stellar luminosity dominates. The top-right middle panel of Figure 9 shows the radial evolution of the massive protostars. The difference in the early radial evolution for these stars is due to their different accretion histories since the accretion of material alters the stellar entropy distribution (Hosokawa & Omukai 2009). In agreement, observations of massive protostars by Ginsburg et al. (2017) find that massive stars are likely bloated as they accrete most of their mass. Until winds become important, the accretion rate is higher for runs ROF$\mu_\phi \infty$ and ROFW$\mu_\phi \infty$ and therefore it is more bloated at early times as compared to runs ROF$\mu_\phi 2$ and ROFW$\mu_\phi 2$. Likewise, when the winds are launched (at around $\sim 20\,M_\odot$) the massive stars are already contracting to the zero-age main sequence (ZAMS) so the reduced (increased) accretion flow in run ROFW$\mu_\phi \infty$ (ROFW$\mu_\phi 2$) has a negligible effect on the radial evolution of the massive (proto)stars. The top-right-hand and bottom-right-hand panels show the accretion timescales, $t_{acc} = M_\star / \dot{M}_\star$, and Kelvin–Helmholtz timescales, $t_{KH} = GM_\star^2 / R_\star L_\star$, respectively. Once the star is sufficiently massive we find that $t_{KH} < t_{acc}$ owing to the high stellar luminosity and contraction to the main sequence.

3.5. Massive Star Wind Properties

The wind mass-loss rates following Equations (14) and (15) (top-left panel), wind velocities (bottom-left panel), stellar effective temperature (center-top panel), stellar radius
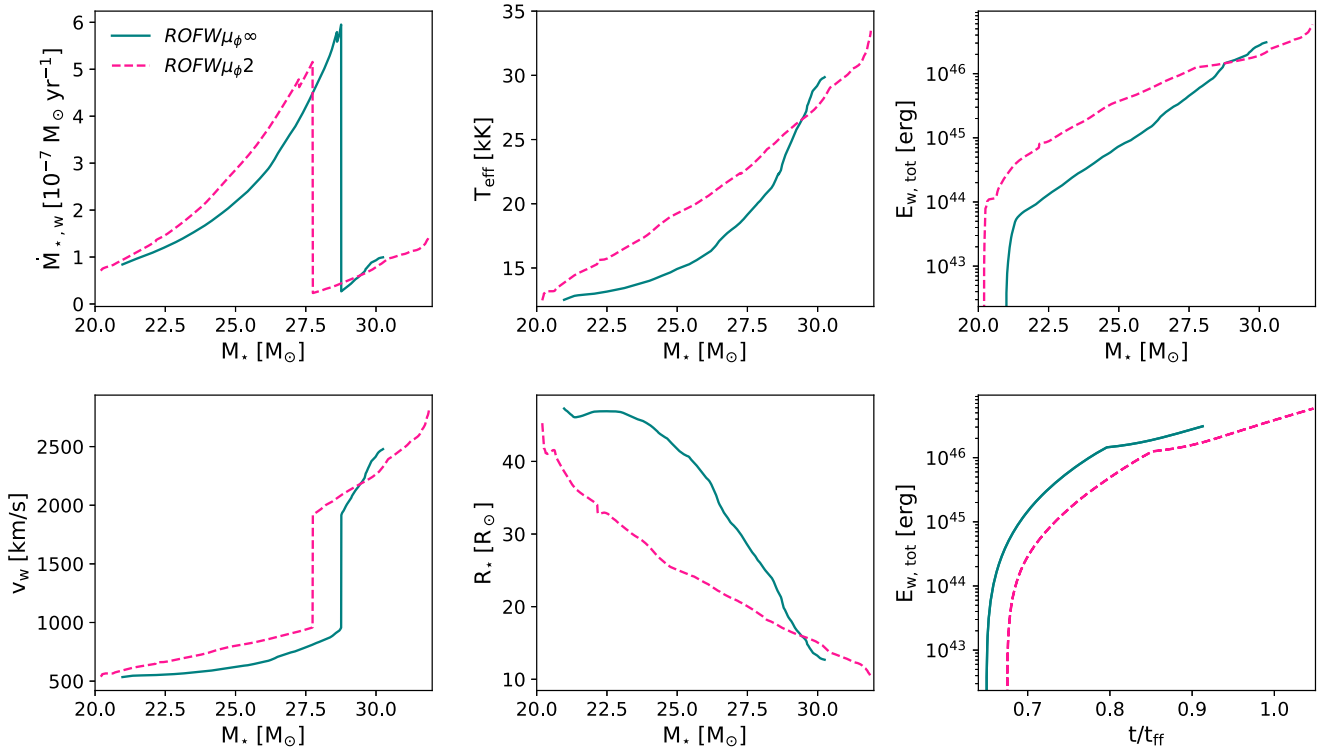
Figure 11. Stellar wind properties as a function of primary stellar mass for runs ROFW$\mu_\phi\infty$ (solid teal lines) and ROFW$\mu_\phi 2$ (dashed pink lines). The top-left panel and bottom-left panel show the wind mass-loss rates and wind velocities following the formulae presented in Section 2.4.3 when the star has $T_{eff} \geqslant 12.5$ kK, following Vink et al. (2001). The top-center and bottom-center panels show the primary star's effective temperature and radius, respectively. The top-right and bottom-right panels show the total integrated wind kinetic energy as a function of stellar mass and simulation time, respectively.

(center-bottom panel), and integrated wind kinetic energy ($E_{w,tot} = \int \frac{1}{2}\dot{M}_w v_w^2 \, dt$, top-right panel) are shown in Figure 11 as a function of stellar mass for the primary star, considering only stellar masses at which the effective temperature is $\gtrsim 12.5$ kK (i.e., hot enough so that winds are launched) for runs ROFW$\mu_\phi\infty$ and ROFW$\mu_\phi 2$. The bottom-right panel also shows the integrated wind kinetic energy ($E_{w,tot}$) as a function of simulation time for comparison.

Initially, the wind mass-loss rates and wind velocities are on the cool side of the bistability jump, as described in Section 2.4.3 and Vink et al. (2001), and are of order $\dot{M}_{\star,w} \sim 10^{-7} \, M_\odot \, yr^{-1}$. When winds are initially launched the wind velocities are relatively low (i.e., $v_w \sim 500 \, km \, s^{-1}$) due to the stars' bloated radii; however, the wind velocities steadily increase to $\sim 10^3 \, km \, s^{-1}$ as the protostars contract to the ZAMS. These quantities steadily increase until the stellar mass reaches $\sim 29 \, M_\odot$ for run ROFW$\mu_\phi\infty$ and $\sim 28 \, M_\odot$ for run ROFW$\mu_\phi 2$ because the stars transition to the hot side of the bistability jump, thereby causing the mass-loss rates to drop by a factor of ~ 5 and the wind velocities to increase by a factor of ~ 2 when this transition occurs. After this transition the mass-loss rates and wind velocities steadily increase as the stars continue to contract to the ZAMS.

The primary star in run ROFW$\mu_\phi 2$ transitions to the hot side of the bistability jump at a lower stellar mass as compared to run ROFW$\mu_\phi\infty$, because the overall stellar accretion rate is lower throughout the simulation time, thereby allowing the star more time to contract to the ZAMS. Eventually, since the growth rate of the massive star in run ROFW$\mu_\phi\infty$ is diminished due to wind feedback, the wind mass-loss rate and wind velocity for run ROFW$\mu_\phi\infty$ become larger than that of run

ROFW$\mu_\phi 2$, because the massive star, at the same stellar mass, has a smaller radius and therefore a higher effective temperature and luminosity. Hence, we find that the wind properties are highly dependent on the protostellar evolution of the massive star and they evolve with time and stellar mass. Future studies that include wind feedback in the context of massive star formation should account for these effects rather than treat the mass-loss rates and wind velocities as a constant value, which has been neglected in previous theoretical studies modeling wind-bubble formation (e.g., Geen et al. 2020, 2021).

As described in Section 3.2, sustained and expanding wind bubbles in run ROFW$\mu_\phi\infty$ form earlier than those in run ROFW$\mu_\phi 2$. Comparison of the total injected wind energy (lower-right panel) as a function of simulation time versus this quantity as a function of stellar mass (top-right panel) shows that winds from the massive protostar are initially launched for run ROFW$\mu_\phi\infty$ earlier than that of ROFW$\mu_\phi 2$. This earlier onset of wind feedback results in a greater amount of wind energy injected as a function of time even though the total injected wind energy for run ROFW$\mu_\phi 2$ is larger as a function of stellar mass due to the faster contraction for the massive protostar. However, since wind feedback reduces accretion onto the massive protostar in run ROFW$\mu_\phi\infty$ earlier than run ROFW$\mu_\phi 2$ the massive protostar begins to contract more quickly than the protostar in run ROFW$\mu_\phi 2$ at $\sim 29 \, M_\odot$.

3.6. Stellar Feedback Comparison

Figure 12 compares the rate of momentum (left panel) and energy (right panel) injection from radiation, collimated outflows, and stellar winds for runs ROFW$\mu_\phi\infty$ and ROFW$\mu_\phi 2$ as a function of primary stellar mass. Here, the rate of momentum deposited is
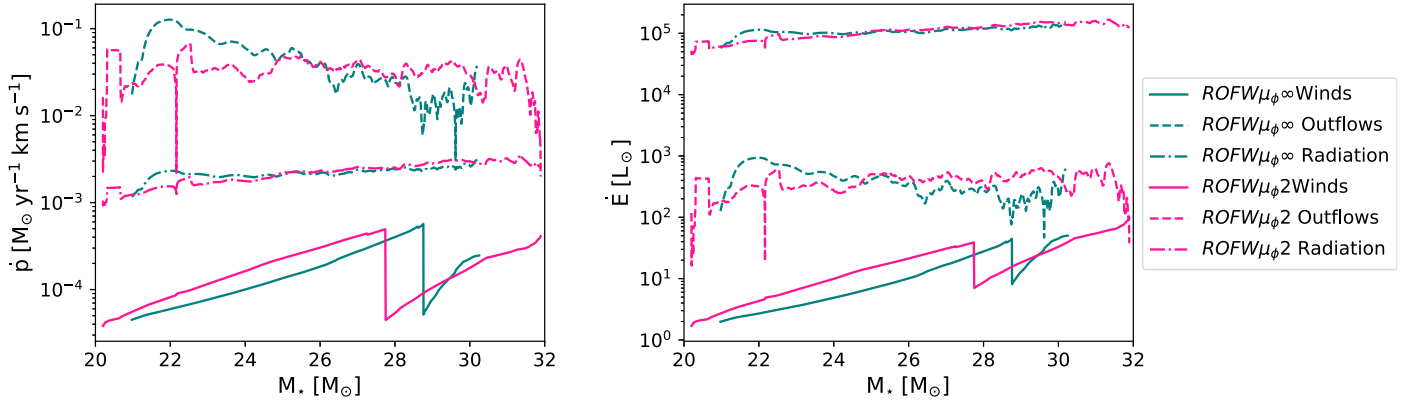
Figure 12. Stellar feedback momentum (left panel) and energy (right panel) deposition rates as a function of primary stellar mass for stellar winds (solid lines), direct radiation including contributions from both the internal (stellar) and accretion luminosities (dotted–dashed lines), and collimated outflows (dashed lines) for runs ROFW$\mu_\phi\infty$ (teal lines) and ROFW$\mu_\phi 2$ (pink lines), respectively. We show these properties when the star becomes hot enough ($T_{\rm eff} \geqslant 12.5$ kK) to launch isotropic winds following the mass-loss rates formulae from Vink et al. (2001).

$\dot{p}_{\rm rad} = (L_\star + L_{\rm acc})/c$, $\dot{p}_o = \dot{M}_o v_o$, and $\dot{p}_w = \dot{M}_w v_w$ for the direct (stellar+accretion) radiation, outflows, and winds, respectively. Likewise, the rate of energy deposited by these feedback processes are $\dot{E}_{\rm rad} = L_\star + L_{\rm acc}$, $\dot{E}_o = \frac{1}{2}\dot{M}_o v_o^2$, and $\dot{E}_w = \frac{1}{2}\dot{M}_w v_w^2$. We only consider the kinetic energy from winds and outflows because they dominate over the thermal energy injected by these feedback processes (i.e., $\dot{E}_{\rm Th,w} \approx 10^{-3}\dot{E}_{\rm K,w}$ and $\dot{E}_{\rm Th,o} \approx 10^{-2}\dot{E}_{\rm K,o}$ for winds and outflows when the primary star is $\gtrsim 20\, M_\odot$, respectively). These quantities are calculated with the self-consistent primary protostar's properties shown in Figures 9 and 11.

We find that the momentum injected by outflows dominates over the momentum injected by radiation and winds whereas the rate of energy deposited by radiation dominates over that of outflows and winds. Likewise, the momentum and energy injected by outflows is much larger than those injected by stellar winds due to the much higher outflow mass-loss rates even though the wind speeds are higher. Regardless, the size scales of these processes differ. The absorption of the direct radiation field depends on the optical depth of the material it interacts with and the hot gas produced by the shock heating of stellar winds, which is effectively transparent to the stellar radiation field because it reaches temperatures much higher than the dust sublimation temperature ($T_{\rm sub} \approx 1500$ K). As shown in Figures 3 and 4, we find that wind feedback drives low-density bubbles near the star before radiation pressure can drive radiation-pressure-driven bubbles. Therefore, once wind feedback produces these adiabatic wind bubbles most of the stellar radiation will be absorbed in the dense bubble shells.

Collimated outflows are injected near the star, similarly to winds, but only over a small covering angle. The momentum in these outflows entrain material that is eventually ejected from the core. We note that, although the outflows contain more kinetic energy than winds, they are not efficiently thermalized like stellar winds because of the much lower outflow velocities and therefore the majority of the kinetic energy in outflows is likely lost via radiative cooling (Koo & McKee 1992; Rosen et al. 2020, 2021). In contrast, the effect of stellar wind feedback is more localized because the injected fast-flowing wind material is thermalized close to the star and the resulting hot gas expands adiabatically near the massive star. Therefore, as shown by the density distribution near the massive star in Figures 3 and 4, wind feedback affects the gas near the star and

therefore is more effective at reducing the accretion flow onto the massive star at late times for runs ROFW$\mu_\phi\infty$ and ROFW$\mu_\phi 2$. Hence, although the energetics of wind feedback is subdominant, we find that winds may be more effective at halting accretion onto massive stars because they act more localized as compared to radiation and outflows.

### 3.7. Entrained Wind Material and Outflows

As noted in Section 2.4 we add passively advected scalars (i.e., tracer fields) to the wind and outflow material that is injected, which is used to measure $\rho_{\rm w}$ and $\rho_{\rm OF}$ precisely for each cell. We define entrained wind and entrained outflow material as consisting of all cells whose mass contains at least 0.005% and 5% of the launched wind and outflow material, respectively (i.e., cells where $f_{\rm t,w} = \rho_{\rm w}/\rho \geqslant 5 \times 10^{-5}$ and $f_{\rm t,OF} = \rho_{\rm w}/\rho \geqslant 5 \times 10^{-2}$). We choose a much lower tracer fraction ($f_{\rm t,w}$) for winds as compared to outflows, because the wind mass-loss rates are several orders of magnitude lower than the launched outflow mass-loss rates.

Figure 13 shows the evolution of the surface density of the entrained wind material for runs ROFW$\mu_\phi\infty$ (top row) and ROFW$\mu_\phi 2$ (bottom row). We note that we do not impose any temperature cuts when integrating over cells that contain wind material and therefore we are highlighting the advection of the wind material rather than only the hot energy-driven wind bubbles discussed in Section 3.2. These panels demonstrate that the core and outflow material that is entrained by winds has a roughly bipolar morphology that expands as the primary star grows in mass. We compare these with the evolution of the surface density of the entrained molecular outflows, as shown in Figure 14, which also has a bipolar morphology due to the collimated structure of the outflows that are launched by the primary star.

Comparison of these two figures shows that the wind material primarily expands along the low-density gas that is carved out by outflows even though the stellar winds are launched isotropically. Additionally, comparison of the last column in Figure 13 shows that the entrained wind material for run ROFW$\mu_\phi 2$ encompasses a larger volume than run ROFW$\mu_\phi\infty$. This suggests that the wind material undergoes the magnetic levitation effect similar to the entrained outflows, as shown in Figure 14, which was first described in Rosen & Krumholz (2020).
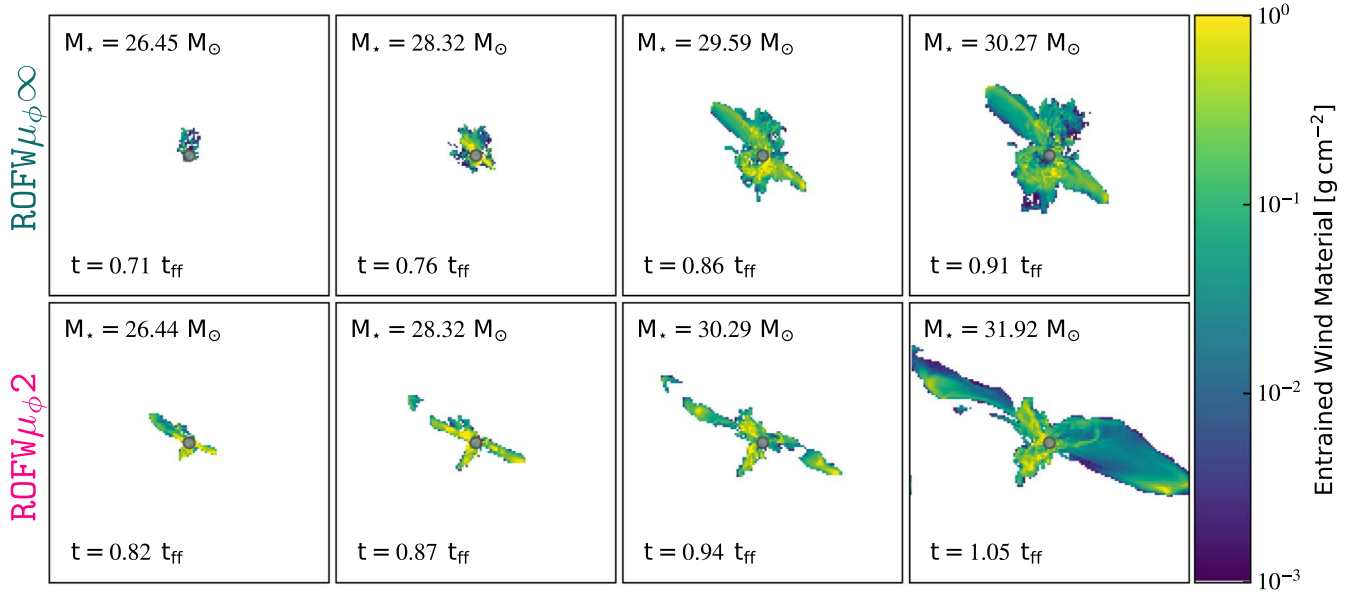
Figure 13. Projections of the density of the entrained wind material along the y–z plane that are moving away from the primary star ($v_{\mathrm{rad}} > 0$) for runs ROFW$\mu_\phi \infty$ (top row) and ROFW$\mu_\phi 2$ (bottom row). Each panel is $(0.4 \, \mathrm{pc})^2$.
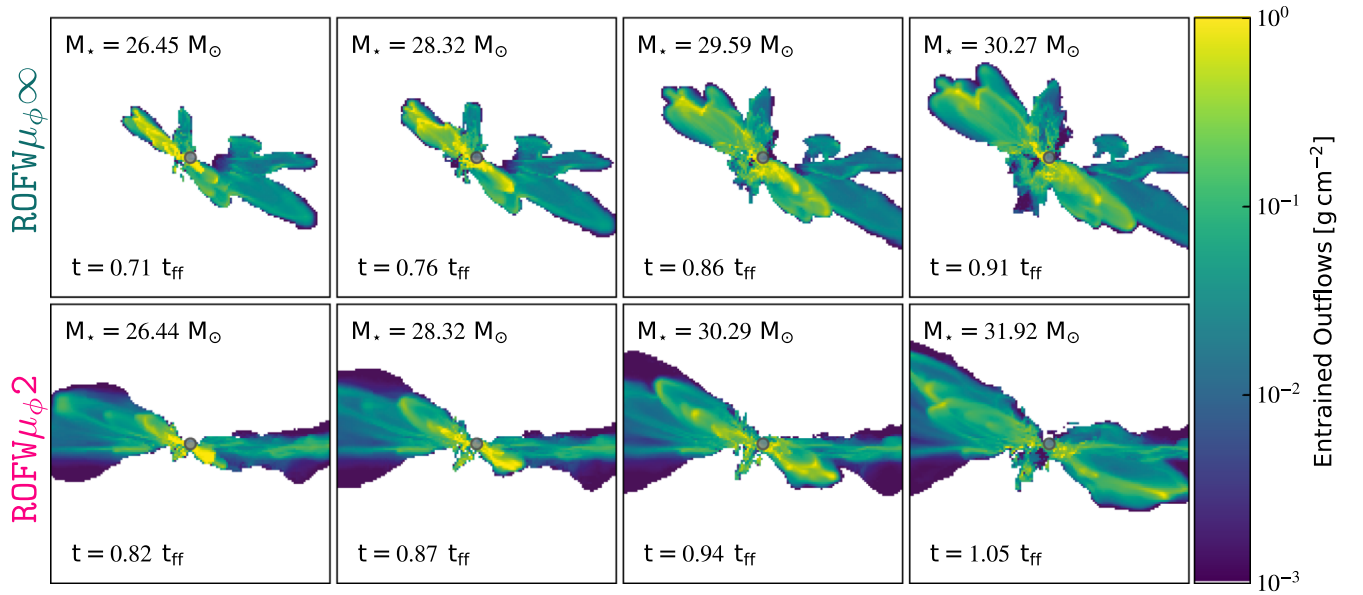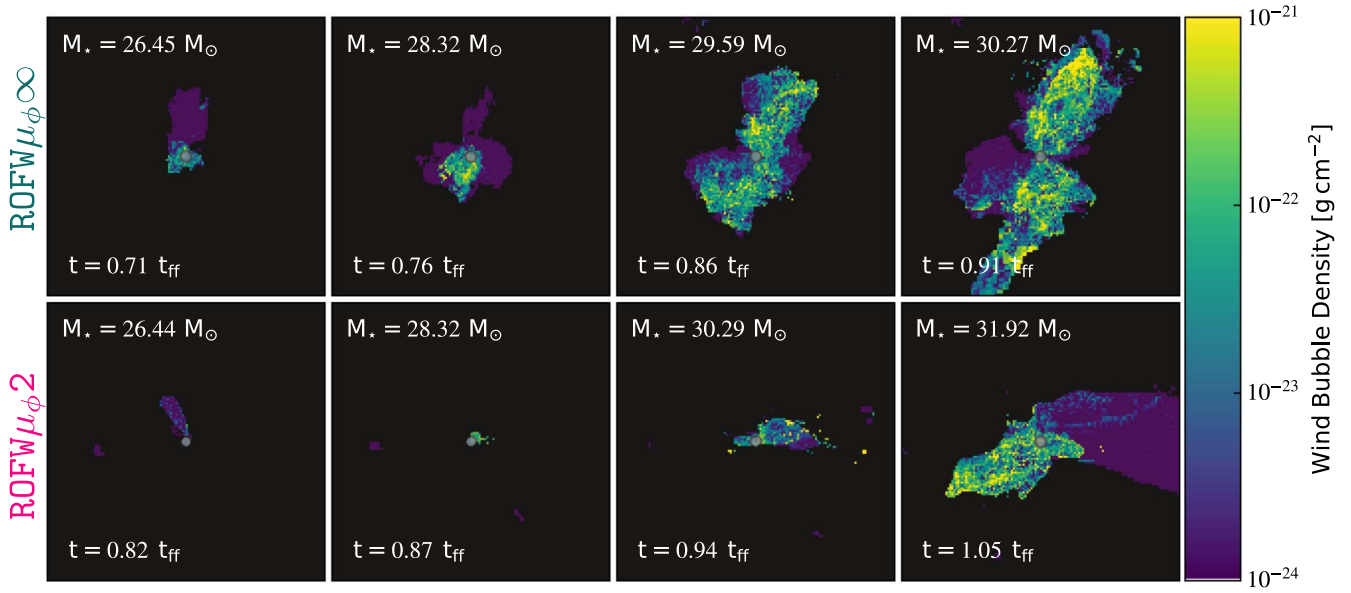

Figure 14. Projections of the density of the entrained outflow material along the y–z plane that are moving away from the primary star ($v_{\mathrm{rad}} > 0$) for runs ROFW$\mu_\phi \infty$ (top row) and ROFW$\mu_\phi 2$ (bottom row). Each panel is $(0.4 \, \mathrm{pc})^2$.

Figure 13 considered all gas that is entrained by the wind material injected by the massive star. However, as described in Section 3.2, we found that the thermalization of stellar winds leads to hot gas that adiabatically expands, leading to hot wind bubbles that eventually reduce the accretion rate onto the massive star. In order to determine if these hot wind bubbles preferentially expand along the same direction as the low-density gas carved out by outflows, we show projections of the mass-weighted density of the hot and warm gas ($T \geqslant 10^4$ K) generated by stellar wind feedback in Figure 15 for runs ROFW$\mu_\phi \infty$ (top row) and ROFW$\mu_\phi 2$ (bottom row). We choose a temperature cutoff of $T \geqslant 10^4$ K because, even though the shock-heated gas produced by wind feedback has $T \geqslant 10^6$ K, this gas will eventually mix with the surrounding cool turbulent gas as it expands that then rapidly cools via turbulent mixing

and conduction (Rosen et al. 2014; Lancaster et al. 2021b). These projections show that the edges of the bubbles are highly turbulent, thereby confirming that turbulent mixing occurs at the hot–cold interface of the bubble shells.

We find that the wind-driven bubbles are roughly bipolar but do not lie along the same orientation as the majority of the entrained wind and outflow material. Likewise, the wind-bubble lobes for the last snapshot of run ROFW$\mu_\phi \infty$ show pinched morphology near the star due to the shielding of the accretion disk. This is less apparent for run ROFW$\mu_\phi 2$ because a substantial accretion disk does not form due to magnetic braking of the infalling material. Regardless, the wind bubble in run ROFW$\mu_\phi 2$ is not spherical and instead is elongated. Comparison of Figures 14 and 15 shows that these lobes do not lie along the same direction as the entrained outflows. Hence,

Figure 15. Projections of the density of the wind bubbles along the y–z plane that are moving away from the primary star ($v_{\mathrm{rad}} > 0$) for runs ROFW$\mu_\phi\infty$ (top row) and ROFW$\mu_\phi 2$ (bottom row) for gas with $T \geqslant 10^4$ K. Each panel is $(0.15\ \mathrm{pc})^2$.
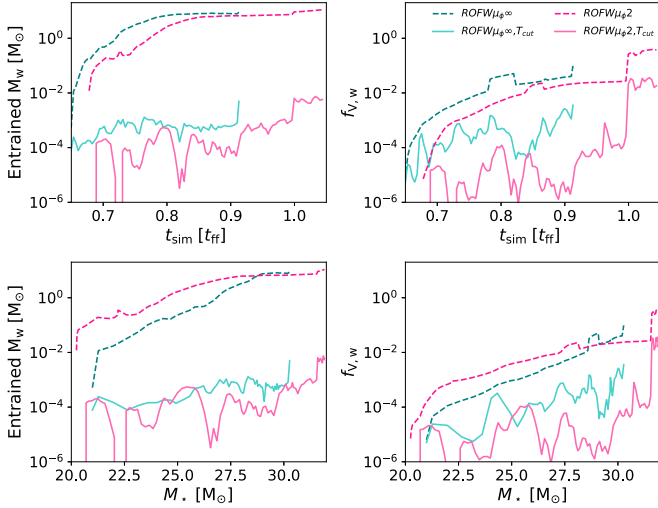
Figure 16. Entrained wind material (left panels) and wind material volume-filling fraction (right panels) as a function of simulation time (top row) and primary stellar mass (bottom row). The lines show where these quantities contain 5×10^{-3}% of wind material. The dark teal and dark pink dashed lines consider all gas for runs ROFW$\mu_\phi\infty$ and ROFW$\mu_\phi 2$, respectively. The light teal and light pink solid lines only consider gas with $T \geqslant 10^4$ K for runs ROFW$\mu_\phi\infty$ and ROFW$\mu_\phi 2$, respectively.

we find that wind material more easily expands along regions where outflow feedback carves out low-density gas but that the hot wind bubbles produced by the shock heating of stellar winds do not primarily expand along the same direction and are instead more localized near the star. Additionally, the hot gas produced by wind feedback preferentially expands along directions that are unimpeded by the dense circumstellar material near the massive star.

We quantify these effects in Figure 16, which shows the entrained wind material (left column) and its volume-filling fraction (right column) as a function of simulation time (top panels) and primary stellar mass (bottom panels) for runs ROFW$\mu_\phi\infty$ and ROFW$\mu_\phi 2$. We calculate the volume-filling fraction by summing over all cells whose mass contains

launched wind material normalized to the initial core volume: $f_{\mathrm{w,V}} = \sum_i dV_{\mathrm{w},i}/V_{\mathrm{core,init}}$, where $V_{\mathrm{core,init}} = \frac{4}{3}\pi R_c^3$. The dotted–dashed lines consider all cells with $f_{\mathrm{t,w}} = \rho_{\mathrm{w}}/\rho \geqslant 5 \times 10^{-5}$ whereas the solid lines only consider cells with $T \geqslant 10^4$ K (i.e., corresponding to the wind bubbles shown in Figure 15). This figure demonstrates that entrained wind material consists of primarily cold ($T < 10^4$ K) gas that encompasses a larger volume than the hot adiabatic wind bubbles. The hot ($T \gtrsim 10^4$ K) wind bubbles encompass a very small volume-filling fraction in comparison because they are initially crushed by the surrounding infalling gas, but once the massive protostar reaches $\sim 30\,M_\odot$ the bubbles exhibit sustained growth and increase in size. At this point for run ROFW$\mu_\phi 2$ the rapid bubble expansion transitions to a more spherical morphology because this simulation does not form a noticeable accretion disk.

3.8. Role of Magnetic Tension in Combating Wind Feedback

In this work we found that magnetic fields have a direct influence on the importance of wind feedback in massive star formation. As noted before, analytic theory and numerical simulations have demonstrated that the fast wind material becomes thermalized and the resulting gas expands adiabatically due to its high temperature (Weaver et al. 1977; Koo & McKee 1992; Rosen et al. 2021). However, this effect is diminished at early times for run ROFW$\mu_\phi 2$ as compared to run ROFW$\mu_\phi\infty$, which does not include magnetic fields.

Figure 17 shows thin-density-weighted projections of the ratio of the magnetic pressure (P_{B}) to thermal gas pressure (P_{gas}) for run ROFW$\mu_\phi 2$ as a function of simulation time. These panels show that throughout most of the simulation (once winds are launched) the material near the massive star has $P_{\mathrm{B}} \gg P_{\mathrm{gas}}$. Eventually regions near the massive star (i.e., when we have wind-driven bubbles that expand away from the star) have thermal gas pressure much larger than the magnetic pressure. Hence, until the winds become significant the magnetic tension associated with the magnetized material near the star reduces the thermalization of the stellar wind material
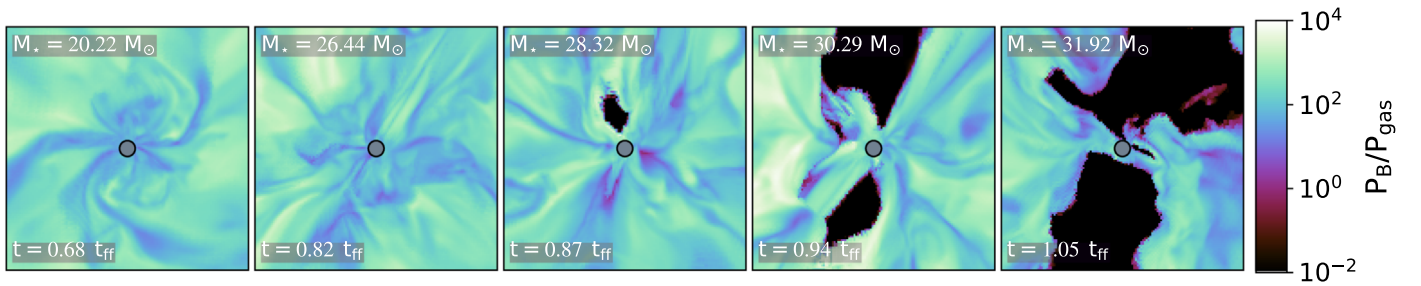
Figure 17. Thin-density-weighted projections of the ratio of the magnetic pressure to thermal gas pressure (P_B/P_{gas}) for run ROFWμ_ϕ2. Each panel is (5000au)^2 in area and the projection is taken over a depth of 500 au, with the massive star, denoted by the gray circle, at the center. Each projection is oriented such that the mass-weighted angular momentum axis of the gas within a radius of 500 au from the massive star points out of the page.

and also confines the expansion of the resulting hot gas. Therefore, we find that confinement due to magnetic tension likely reduces the production and expansion of wind-driven bubbles that form via wind feedback, which are more apparent in run ROFW$\mu_\phi\infty$ since the wind-driven bubbles are launched at a lower stellar mass.

In order to determine how magnetic fields influence wind feedback we compare two identical simulations to runs ROFμ_ϕ2 and ROFWμ_ϕ2 but include a magnetic field strength that is a factor of 10 lower, yielding an initial $\mu_\phi = 20$ (runs ROFμ_ϕ20 and ROFWμ_ϕ20), which acts as an intermediate case to the magnetized and unmagnetized cores described throughout this work. Figure 18 shows the growth rate for the massive star that forms in all of the simulations as a function of simulation time. As described in Section 3.4 we found that wind feedback reduces the mass growth of the primary star when the core is not magnetized, but the mass growth is slightly enhanced when it is. Comparison of runs ROFμ_ϕ20 and ROFWμ_ϕ20 with the other simulations shows that a weaker magnetic field reduces the mass growth compared to the nonmagnetic case but increases it compared to the magnetic case. When winds become important for run ROFWμ_ϕ20 we find that the mass growth rate is very similar to the mass growth of the massive star in run ROFμ_ϕ20, suggesting that if the core is weakly magnetized then winds do not enhance or decrease the growth rate of the massive star, at least for the time simulated here.

4. Discussion

The purpose of this work is to understand how feedback from isotropic radiatively driven stellar winds, in concert with feedback from collimated outflows and radiation pressure, affect the formation of massive stars that form from the gravitational collapse of unmagnetized and magnetized massive prestellar cores. Most notably, we find that wind feedback significantly reduces accretion onto massive stars that form from the collapse of unmagnetized prestellar cores. However, for collapsing magnetized cores we find that accretion onto massive stars is slightly enhanced, before it begins to taper off once winds are powerful enough to launch adiabatic wind bubbles since magnetic tension in the surrounding material inhibits their growth at early times. Additionally, we find that the wind-blown bubbles that emanate are not spherical and are instead roughly bipolar because the hot gas is pinched by the dense circumstellar material or disk that forms around the massive star. In this section, we discuss a new phenomenon, called the "wind tunnel effect," that describes this bipolar structure of the wind-driven bubbles in Section 4.1, the
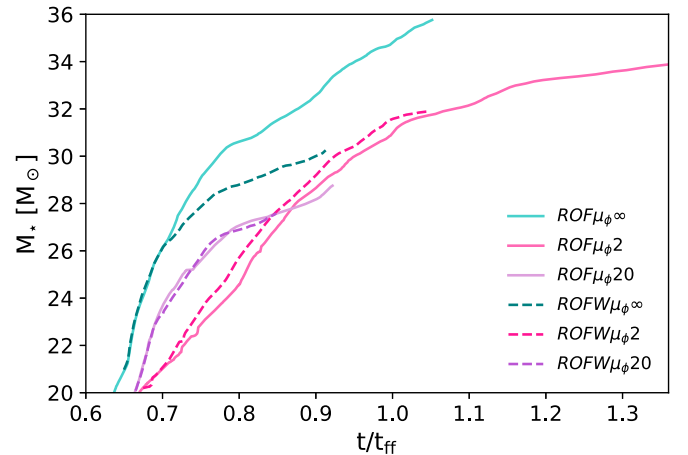

Figure 18. Primary protostar mass as a function of simulation time for runs ROF$\mu_\phi\infty$, ROFW$\mu_\phi\infty$, ROFμ_ϕ2, ROFWμ_ϕ2, ROFμ_ϕ20, and ROFWμ_ϕ20.

implications of studying these structures with Chandra and future X-ray telescopes in Section 4.2, and we address the caveats of our simulations in Section 4.3.

4.1. The "Wind Tunnel Effect"

Previous numerical work that modeled the role of radiation pressure in massive star formation, but neglected wind feedback, demonstrated that the presence of an optically thick accretion disk reduces the effects of radiative acceleration in the radial direction, leading to the "flashlight effect" in which the radiative flux escapes along the polar axis and into the polar cavities, launching radiation-pressure-dominated bubbles above and below the star (e.g., Yorke & Sonnhalter 2002; Krumholz et al. 2009; Rosen et al. 2016, 2019). The simulations presented here also include isotropic wind and collimated outflow feedback from massive stars, and show a similar effect occurs for the hot shock-heated gas ($T \gtrsim 10^6$ K) produced by stellar wind feedback that undergoes adiabatic expansion (i.e., $P\,dV$ work). The hot gas preferentially expands in directions perpendicular to the accretion disk or dense circumstellar material since the gas density is much lower along these directions. Hence, we find that the thermalized gas produced by wind feedback experiences the greatest expansion along the polar directions of the massive star, which we term the "wind tunnel effect" in an analogous manner to the "flashlight effect" due to radiative feedback.

This "wind tunnel effect" produces hot gas lobes that are pinched by the dense accretion disk or dense circumstellar material, thereby resulting in an hour glass morphology, as
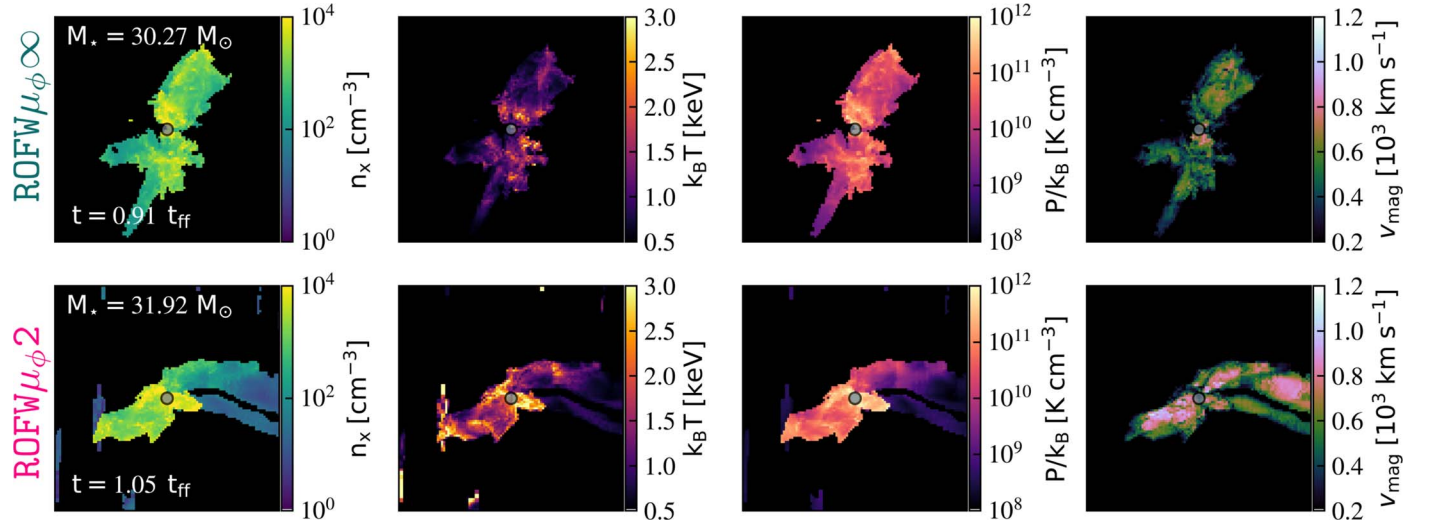
Figure 19. Projections of the number density (left column), temperature (center-left column), pressure (center-right column), and velocity magnitude (right column) of the hot gas within the wind bubbles along the y–z plane of the final snapshots for runs ROFW$\mu_\phi\infty$ (top row) and ROFW$\mu_\phi2$ (bottom row) considering only gas with $T \geqslant 0.5$ keV ($T \geqslant 5.8 \times 10^6$ K). Each panel is $(0.15 \text{ pc})^2$.

shown in Figures 5, 6, and 15 for runs ROFW$\mu_\phi\infty$ and ROFW$\mu_\phi2$, respectively, rather than a spherical bubble as would be expected for isotropic wind feedback in a uniform medium (Weaver et al. 1977; Koo & McKee 1992). By comparing runs ROFW$\mu_\phi\infty$ and ROFW$\mu_\phi2$ with identical simulations that neglect wind feedback (runs ROF$\mu_\phi\infty$ and ROF$\mu_\phi2$), we find that the "wind tunnel effect" occurs before radiation pressure becomes strong enough to launch the radiation-pressure-dominated bubbles. Regardless, the morphology of these two effects are similar, and the result is that feedback from radiation and winds, both of which are launched isotropically, lead to asymmetric low-density lobes that expand as the massive star grows in mass. When magnetic fields are included we find that the "wind tunnel effect" is delayed and the wind-driven lobes are smaller in volume than the nonmagnetic case, at a given stellar mass, because the expanding wind bubbles are confined by magnetic tension. This similar effect was found for the radiation-pressure-dominated bubbles presented in Rosen & Krumholz (2020).

One interesting comparison to note here is that the structure of the bipolar wind bubbles expected from massive protostars, as demonstrated in this work, are morphologically similar to those observed for evolved massive stars and interacting massive binaries. For example, the nebulae of evolved massive stars, such as fast-rotating luminous blue variables, typically have a bipolar morphology because equatorial gravity darkening will lead to a higher mass-loss rate and faster wind speed along the poles of the star (Dwarkadas & Owocki 2002; Lobel et al. 2013; Smith 2014). Likewise, some Wolf–Rayet (WR) stars have also been observed to have a bipolar wind-bubble morphology; these structures likely occur if the WR star has undergone a blue supergiant evolutionary phase or experienced binary interactions or mergers during its red supergiant evolutionary phase (Meyer 2021).

4.2. Implications for X-Ray Observations

Extended X-ray emission has been detected for several ultracompact and compact H II regions ($R_{\text{Hii}} \lesssim 0.5$ pc) in the Milky Way (Takagi et al. 2002; Tsujimoto et al. 2006; Anderson et al. 2011; Skinner et al. 2019; Olivier et al. 2021).

This emission likely traces the hot ($T \gtrsim 10^7$ K) thermal plasma generated by the shock heating of stellar winds launched by individual or multiple massive (proto)stars, but the X-ray emission may also be affiliated with the central sources (i.e., the massive protostars that power the winds and nearby low-mass pre-main-sequence stars; Feigelson et al. 2005; Getman et al. 2005). Chandra observations of these compact H II regions found that the emission is dominated by hard X-rays ($\geqslant 3$ keV) and these observations were unable to resolve the stellar sources from the diffuse plasma, thereby leading to confusion (Olivier et al. 2021). The soft X-rays ($\lesssim 3$ keV) were likely highly attenuated by the high column densities ($N_{\text{H}} \gtrsim 10^{23}$ cm^{-2}) of the compact H II regions (Takagi et al. 2002; Tsujimoto et al. 2006; Anderson et al. 2011). In order to shed light on these observations and understand why the detected Chandra X-ray emission is dominated by $\gtrsim 3$ keV photons, we look at the distribution of the hot gas properties with $k_B T_X \geqslant 0.5$ keV ($T_X \geqslant 5.8$ MK) that could be detectable by Chandra.

Figure 19 shows the density-weighted projections of the number density (n_X; left column), temperature ($k_B T_X$; center-left column), thermal pressure ($P_X/k_B = 1.9 n_X T_X$, where the factor of 1.9 assumes that He is doubly ionized and the He mass fraction is 0.25), and velocity magnitude (v_{mag}) of the hot gas produced by the shock heating of stellar winds for the final snapshots for runs ROFW$\mu_\phi\infty$ (top row) and ROFW$\mu_\phi2$ (bottom row). These panels show that this hot gas occupies a small filling factor (f; i.e., the volume of the H II region occupied by the hot shock-heated gas) for the region. Olivier et al. (2021) assume a filling factor $f = 1$ when estimating P_X (i.e., the hot gas fully occupies a sphere with radius $R_{\text{H II}}$); however, we find that $f \approx 0.02$ for both simulations (assuming $R_{\text{Hii}} = 0.075$ pc), suggesting that the hot gas should only occupy a tiny nonspherical fraction of the (assumed) spherical H II regions.

The volume-weighted average wind-bubble properties and intervening core column densities for the final snapshots of runs ROFW$\mu_\phi\infty$ and ROFW$\mu_\phi2$ are listed in Table 2. We use CHIANTI (Dere et al. 1997) to compute the emissivity, $j_\nu(T, Z)$, to obtain the total wind-bubble X-ray luminosity $L_X = 0.9 n_x^2 j(T_X, Z)$,

Table 2
Wind-driven Bubble Properties

	ROFW$\mu_\phi\infty$	ROFWμ_ϕ2
$M_{\star,\mathrm{f}}$ ($M_\odot$)	30.27	31.92
n_X (cm^{-3})[a]	1.16×10^3	1.21×10^3
T_X (keV)[a]	1.19	1.59
P_X/k (K cm^{-3})[a]	4.48×10^9	7.56×10^9
v_{mag} (km s^{-1})[a]	513.5	703.0
f[b]	0.0196	0.0221
N_H (cm^{-2})[d]	1.0×10^{24}	4.5×10^{23}
L_X (10^{33} erg s^{-1})[e]	6.20	9.82
F_X (10^{-13} erg cm^{-2} s^{-1})	4.21	6.66
(0.5–3) keV CPS (s^{-1})[f]	1.083×10^{-8}	1.224×10^{-5}
(3–7) keV CPS (s^{-1})[f]	4.099×10^{-5}	6.808×10^{-4}

Notes.
[a] Volume-weighted quantity.
[b] Hot gas filling factor within a sphere with radius $R = 0.075$ pc centered on the massive star.
[c] Average attenuating column density.
[d] Considering emission only from gas with $kT \geqslant 0.5$ keV.
[e] Unabsorbed flux assuming a distance of $D = 11.1$ kpc ($F_X = L_X/4\pi D^2$).
[f] Photon counts per second. Calculated via WebPIMMs.

where $j(T_X, Z)$ is the integrated total emissivity over the (0.5–7) keV X-ray band, T_X and n_X are the volume-weighted average quantities listed in Table 2, and we assume solar metallicity (Rosen et al. 2014). We compute the flux, $F_X = L_X/(4\pi D^2)$, by assuming a distance of $D = 11.1$ kpc (Zhang et al. 2013; i.e., the distance to the massive star-forming region W49A that had detected X-ray emission in Tsujimoto et al. 2006 and Olivier et al. 2021). The X-ray photon count rates for the soft (0.5–3 keV) and hard (3–7 keV) Chandra wavelength ranges are then computed with WebPIMMS[7] for the Chandra ACIS-I detector[8] and we assume the flux is dominated with thermal bremsstrahlung emission with kT equal to the volume-averaged values listed in Table 2. The resulting values are listed in Table 2. In agreement with the observations mentioned above, we find that the soft X-ray band ($\leqslant 3$ keV) would be undetectable by Chandra due to the high attenuating column densities of the protostellar core ($N_H \gtrsim 4.5 \times 10^{23}$ cm^{-2}) and that the hard X-ray band ($\geqslant 3$ keV) should be more easily detectable.

These results suggest that studying the impact of wind feedback in the early formation of massive stars, when the stars are heavily embedded with $N_H > 10^{23}$ cm^{-2}, is challenging. However, as these H II regions expand and evolve, thereby achieving lower intervening attenuating column densities, the diffuse soft X-ray emission will be less attenuated and should be observable with Chandra. Such emission has been observed for a number of extended H II regions ($R_{\mathrm{HII}} \geqslant$ few pc) that host massive star clusters (Lopez et al. 2011; Townsley et al. 2011; Lopez et al. 2014; Rosen et al. 2014). However, future X-ray telescopes with much greater spatial resolution and sensitivity than Chandra may be able to differentiate the point-like stellar sources from the compact diffuse wind-bubble emission from the compact highly embedded H II regions from massive protostars within the Milky Way.

[7] https://heasarc.gsfc.nasa.gov/cgi-bin/Tools/w3pimms/w3pimms.pl
[8] The ACIS-I detector was chosen because it is better suited to observe compact sources.

4.3. Caveats

In this work, we simulated the impact of stellar feedback from massive protostars that form from the gravitational collapse of *isolated* massive prestellar cores and found that the thermalization of stellar winds (i.e., energy-driven wind feedback) can cause the accretion of material to be quenched when the massive star reaches $\sim 30\,M_\odot$. However, observations have demonstrated that massive stars form in dense, highly dynamical GMCs that are undergoing gravitational collapse, thereby driving converging flows that provide large-scale accretion to the birth sites of massive stars (Williams et al. 2018; Kumar et al. 2020; Rosen et al. 2020; Avison et al. 2021).

The associated ram pressure associated with these inflows will likely make feedback less important for massive star formation (e.g., Kuiper & Hosokawa 2018). Grudic et al. (2022) show that massive stars tend to form later than their low-mass counterparts in GMCs and that they likely form in high-density sites where dynamical accretion occurs. Therefore, our results demonstrate that massive stars $\gtrsim 30\,M_\odot$ likely can not form from the collapse of isolated massive cores that are not undergoing dynamical accretion from its external environment. Hence, future numerical work studying massive star formation should follow how mass is accumulated from the large (GMC) to small scales (birth sites of massive stars). Studies like these can be done with the new STARFORGE project, which is capable of resolving individual star formation within GMCs and includes all of the relevant stellar feedback processes, and which is now studying this in more detail (Grudic et al. 2021, 2022; Guszejnov et al. 2022).

In the simulations presented here, which neglected nonideal MHD effects, we find that magnetic fields have a direct influence on the importance of wind feedback in massive star formation. Since these simulations are in the ideal limit, they assume that the magnetic field lines are well coupled to the gas and therefore the magnetic field strength is amplified as the core contracts. This leads to a greater magnetic field strength near the massive protostar, where the density is high, thereby resulting in a larger magnetic tension that can inhibit or delay the growth of the adiabatic wind bubbles (e.g., Rosen & Krumholz 2020). Nonideal effects, such as ambipolar diffusion and ohmic dissipation, likely weaken the magnetic field strength near the massive star (Kölligan & Kuiper 2018; Zhao et al. 2020), thereby making magnetic tension less important as the system evolves and the star grows in mass. Hence, future work that explores the importance of wind feedback in massive star formation should include these effects. We note that ideal MHD effects are likely a good approximation for the wind bubbles simulated here since the thermalized gas is fully ionized. However, nonideal MHD effects may weaken the magnetic field near the accreting protostar before winds are launched, thereby reducing the magnetic tension that is responsible for suppressing the growth of the adiabatic wind bubbles which eventually inhibit accretion.

Additionally, we note that the stellar wind modeling used in the simulations presented here assume that winds are initially launched once the protostar reaches an effective temperature of ~ 12.5 kK following the prescription by Vink et al. (2001), which modeled the wind properties of nonaccreting massive stars based on their stellar properties and interpolated their model to lower temperatures. Hence, it still remains uncertain when massive (proto)stars begin to experience mass loss due to

radiation pressure in their atmospheres. However, Vink (2018) modeled the stellar wind properties for very massive, bloated stars with $T_{\rm eff} = 15$ kK and found that radiation pressure was able to launch slow winds ($\sim$few $\times$ 10^2 km s^{-1}) with high mass-loss rates due to their bloated radii and high luminosities. Therefore, we expect stellar winds should initially be launched during the accretion phase for massive protostars due to their high luminosities ($\sim 10^5$–$10^6 L_\odot$). Regardless, future wind modeling should study how winds can be launched when the massive protostar is actively accreting and contracting to the main sequence.

Another important detail about radiatively driven stellar winds that is neglected in these simulations are the small-scale density inhomogeneities (i.e., clumping) within the stellar wind that are a result of the strong, intrinsic instability of line driving (i.e., the line-deshadowing instability; Smith 2014; Sundqvist et al. 2018; Brands et al. 2022). This feature of radiatively driven stellar winds is still poorly understood, therefore we were not able to properly include this effect in our subgrid wind model. We note that future studies should consider including wind clumping in their mass-loss prescriptions because asymmetric mass loss will likely introduce additional asymmetries in the wind bubbles that form around massive protostars.

Finally, our subgrid wind-launching model only included contributions from the stellar surface. Kee et al. (2018) and Kee & Kuiper (2019) find that UV radiation from main-sequence-like massive stars can also ablate the accretion disk leading to an extended supersonic disk wind near the star, thereby enhancing the overall mass-loss rate of the star–disk system. For main-sequence massive stars, they find that the disk ablation rate scales as $\dot{M}_{\rm abl} \sim 6.5 \dot{M}_{\star,\rm w}$ and therefore UV-driven disk ablation should reduce the final stellar masses by 15%. Our results suggest disk ablation may occur earlier as the massive star contracts to the main sequence, since winds should be launched before the star reaches the main sequence. However, modeling the launching of UV-driven disk winds self-consistently for the simulations discussed in this work requires extremely high resolution ($\sim R_\star$), as demonstrated by Kee & Kuiper (2019), and therefore is not currently computationally tractable. However, future work may be able to incorporate the results of Kee & Kuiper (2019) as a disk wind subgrid model in addition to the subgrid wind model presented here. However, it remains unclear how efficient disk ablation is before the massive star reaches the main sequence.

5. Conclusions

In this work, we performed a series of 3D RMHD simulations of the gravitational collapse of isolated dense massive prestellar cores to determine how magnetic fields, turbulence, and stellar feedback from radiation pressure, collimated protostellar outflows, and isotropic radiatively driven winds affect the formation of massive stellar systems. This is the first study of massive star formation to include stellar wind feedback, along with the stellar and dust-reprocessed radiation pressures and collimated outflows, in the context of a realistic, turbulent medium and self-consistent feedback evolution during star formation. By following the impact of stellar wind feedback we have investigated the production and expansion of adiabatic wind-driven bubbles in massive star formation with and without magnetic fields.

We reach the following conclusions:

1. Radiatively driven stellar winds are initially launched when massive stars are still actively accreting and contracting to the ZAMS. For the simulations presented here winds are initially launched when the star reaches $\sim 20 \ M_\odot$.

2. The mass-loss rates and wind velocities evolve as the stars grow in mass and contract to the ZAMS. Therefore, protostellar evolution must be taken into account when modeling stellar wind feedback in massive star formation simulations.

3. We find that the kinetic energy and momentum injected by stellar winds is subdominant to that injected by stellar radiation and collimated outflows. Regardless, we find that winds are more likely to reduce the accretion flow onto massive stars when they are sufficiently massive.

4. We find that, for both magnetized and unmagnetized cores, the kinetic energy injected by stellar winds from massive stars produces hot shock-heated gas that expands adiabatically and launches expanding wind-driven bubbles or lobes that are asymmetrical and bipolar in morphology. We name this phenomenon the "wind tunnel effect," which is analogous to the "flashlight effect" commonly seen in massive star formation simulations that only include radiative feedback.

5. We find that the "wind tunnel effect" occurs before the "flashlight effect" when wind feedback is included. Like the "flashlight effect," the hot gas produced by the shock heating of stellar winds preferentially expands along regions where the density is lowest and therefore the presence of an accretion disk or dense circumstellar material pinches the expanding gas causing it to expand along the bipolar directions of the massive star.

6. By comparing identical simulations of the collapse of magnetized and unmagnetized prestellar cores that form massive stars we find that the wind-driven bubbles are launched at a lower stellar mass when magnetic fields are not included (at $\sim 27 \ M_\odot$ versus $\sim 31 \ M_\odot$). We suggest that magnetic tension near the star delays the growth of these bubbles until stellar wind feedback is strong enough to overcome the magnetic tension, thereby leading to the sustained expansion of adiabatic wind bubbles.

7. For unmagnetized cores we find that wind feedback can greatly inhibit the accretion of material onto massive stars once stellar winds are significant. In contrast, for magnetized cores we find that wind feedback initially enhances the growth rate of massive stars but once wind feedback becomes strong enough to launch wind-driven bubbles the accretion rate begins to decrease. Our results suggest that once stars become sufficiently massive, their strong stellar winds may inhibit accretion onto massive stars at late times.

8. By comparing the entrained wind and outflow material, we find that most of the wind material preferentially follows the low-density gas carved out by outflows. However, we find that the hot wind-driven bubbles are smaller in volume than the entrained wind material. In addition, we find evidence that mixing with the surrounding cooler gas occurs at the shells of the wind-driven bubbles.

9. Given that wind feedback appears to be effective at quenching accretion onto $\sim 30 \ M_\odot$ protostars, our results suggest that stars more massive than this likely form via

larger-scale, high-ram-pressure dynamical inflows from their host cloud to overcome wind feedback.

10. We showed that the diffuse ($\leqslant 3$ keV) X-ray emission is highly attenuated due to the high column densities associated with the massive core and therefore is likely not detectable by Chandra. We do find that the hard ($\geqslant 3$ keV) X-ray emission may be detectable by Chandra in agreement with observations. However, future X-ray telescopes, with a higher sensitivity and better spatial resolution, may be able to study the soft X-ray emission produced by highly embedded massive protostars.

Software: YT (Turk et al. 2011), ORION2 (Li et al. 2012, 2021), HARM^2 (Rosen et al. 2017), CHIANTI (Dere et al. 1997).

ORCID iDs

Anna L. Rosen ⓘ https://orcid.org/0000-0003-4423-0660

References

Anderson, C. N., Hofner, P., Shepherd, D., & Creech-Eakman, M. 2011, AJ, 142, 158
Avison, A., Fuller, G. A., Peretto, N., et al. 2021, A&A, 645, A142
Battersby, C., Ginsburg, A., Bally, J., et al. 2014, ApJ, 787, 113
Behrend, R., & Maeder, A. 2001, A&A, 373, 190
Bertoldi, F., & McKee, C. F. 1992, ApJ, 395, 140
Beuther, H., Gieser, C., Suri, S., et al. 2021, A&A, 649, A113
Beuther, H., Leurini, S., Schilke, P., et al. 2007, A&A, 466, 1065
Beuther, H., Schilke, P., Menten, K. M., et al. 2002, ApJ, 566, 945
Boldyrev, S. 2002, ApJ, 569, 841
Brands, S. A., de Koter, A., Bestenlehner, J. M., et al. 2022, A&A, 663, A36
Butler, M. J., & Tan, J. C. 2012, ApJ, 754, 5
Cao, Y., Qiu, K., Zhang, Q., et al. 2019, ApJS, 241, 1
Caselli, P., & Myers, P. C. 1995, ApJ, 446, 665
Castor, J., McCray, R., & Weaver, R. 1975, ApJL, 200, L107
Cho, J., & Lazarian, A. 2003, MNRAS, 345, 325
Commerçon, B., González, M., Mignon-Risse, R., Hennebelle, P., & Vaytet, N. 2021, A&A, 658, A52
Courant, R., Friedrichs, K., & Lewy, H. 1967, IBMJ, 11, 215
Crutcher, R. M. 2012, ARA&A, 50, 29
Cunningham, A. J., Klein, R. I., Krumholz, M. R., & McKee, C. F. 2011, ApJ, 740, 107
Dale, J. E., Ngoumou, J., Ercolano, B., & Bonnell, I. A. 2014, MNRAS, 442, 694
Dere, K. P., Landi, E., Mason, H. E., Monsignori Fossi, B. C., & Young, P. R. 1997, A&AS, 125, 149
Dwarkadas, V. V., & Owocki, S. P. 2002, ApJ, 581, 1337

Feigelson, E. D., Getman, K., Townsley, L., et al. 2005, ApJS, 160, 379
Fielding, D. B., McKee, C. F., Socrates, A., Cunningham, A. J., & Klein, R. I. 2015, MNRAS, 450, 3306
Gatto, A., Walch, S., Naab, T., et al. 2017, MNRAS, 466, 1903
Geen, S., Bieri, R., Rosdahl, J., & de Koter, A. 2021, MNRAS, 501, 1352
Geen, S., Pellegrini, E., Bieri, R., & Klessen, R. 2020, MNRAS, 492, 915
Getman, K. V., Flaccomio, E., Broos, P. S., et al. 2005, ApJS, 160, 319
Ginsburg, A., Bally, J., Barnes, A., et al. 2018, ApJ, 853, 171
Ginsburg, A., Bally, J., Battersby, C., et al. 2015, A&A, 573, A106
Ginsburg, A., Goddi, C., Kruijssen, J. M. D., et al. 2017, ApJ, 842, 92
Goldreich, P., & Sridhar, S. 1995, ApJ, 438, 763
Grudic, M. Y., Guszejnov, D., Hopkins, P. F., Offner, S. S. R., & Faucher-Giguere, C.-A. 2021, MNRAS, 506, 2199
Grudic, M. Y., Guszejnov, D., Offner, S. S. R., et al. 2022, MNRAS, 512, 216
Guszejnov, D., Markey, C., Offner, S. S. R., et al. 2022, MNRAS, 515, 167
Helling, C., Winters, J. M., & Sedlmayr, E. 2000, A&A, 358, 651
Hopkins, P. F., Kereš, P. F., Oñorbe, J., et al. 2014, MNRAS, 445, 581
Hopkins, P. F., Rosen, A. L., Squire, J., et al. 2022, MNRAS, 517, 1491
Hosokawa, T., & Omukai, K. 2009, ApJ, 691, 823
Hull, C. L. H., & Zhang, Q. 2019, FrASS, 6, 3
Kee, N. D., & Kuiper, R. 2019, MNRAS, 483, 4893
Kee, N. D., Owocki, S., & Kuiper, R. 2018, MNRAS, 479, 4633
Kölligan, A., & Kuiper, R. 2018, A&A, 620, A182
Koo, B.-C., & McKee, C. F. 1992, ApJ, 388, 93
Kowal, G., & Lazarian, A. 2010, ApJ, 720, 742
Kowal, G., Lazarian, A., & Beresnyak, A. 2007, ApJ, 658, 423
Krumholz, M. R., Klein, R. I., McKee, C. F., & Bolstad, J. 2007, ApJ, 667, 626
Krumholz, M. R., Klein, R. I., McKee, C. F., Offner, S. S. R., & Cunningham, A. J. 2009, Sci, 323, 754
Krumholz, M. R., McKee, C. F., & Bland-Hawthorn, J. 2019, ARA&A, 57, 227
Krumholz, M. R., McKee, C. F., & Klein, R. I. 2004, ApJ, 611, 399
Kuiper, R., & Hosokawa, T. 2018, A&A, 616, A101
Kuiper, R., Yorke, H. W., & Turner, N. J. 2015, ApJ, 800, 86
Kumar, M. S. N., Palmeirim, P., Arzoumanian, D., & Inutsuka, S. I. 2020, A&A, 642, A87
Lancaster, L., Ostriker, E. C., Kim, J.-G., & Kim, C.-G. 2021a, ApJ, 914, 89
Lancaster, L., Ostriker, E. C., Kim, J.-G., & Kim, C.-G. 2021b, ApJ, 914, 90
Leitherer, C., Robert, C., & Drissen, L. 1992, ApJ, 401, 596
Lejeune, T., Cuisinier, F., & Buser, R. 1997, A&AS, 125, 229
Li, P., Cunningham, A., Gaches, B., et al. 2021, JOSS, 6, 3771
Li, P. S., Martin, D. F., Klein, R. I., & McKee, C. F. 2012, ApJ, 745, 139
Li, S., Sanhueza, P., Zhang, Q., et al. 2020, ApJ, 903, 119
Lobel, A., Groh, J. H., Martayan, C., et al. 2013, A&A, 559, A16
Longmore, S. N., Pillai, T., Keto, E., Zhang, Q., & Qiu, K. 2011, ApJ, 726, 97
Lopez, L. A., Krumholz, M. R., Bolatto, A. D., et al. 2014, ApJ, 795, 121
Lopez, L. A., Krumholz, M. R., Bolatto, A. D., Prochaska, J. X., & Ramirez-Ruiz, E. 2011, ApJ, 731, 91
Masunaga, H., & Inutsuka, S.-i. 2000, ApJ, 531, 350
Masunaga, H., Miyama, S. M., & Inutsuka, S.-i. 1998, ApJ, 495, 346
Matzner, C. D., & McKee, C. F. 2000, ApJ, 545, 364
Maud, L. T., Moore, T. J. T., Lumsden, S. L., et al. 2015, MNRAS, 453, 645
Meyer, D.-M.-A. 2021, MNRAS, 507, 4697
Mignon-Risse, R., González, M., Commerçon, B., & Rosdahl, J. 2020, A&A, 635, A42
Mignon-Risse, R., González, M., Commerçon, B., & Rosdahl, J. 2021, A&A, 652, A69
Mueller, K. E., Shirley, Y. L., Evans, N. J., II, & Jacobson, H. R. 2002, ApJS, 143, 469
Myers, A. T., McKee, C. F., Cunningham, A. J., Klein, R. I., & Krumholz, M. R. 2013, ApJ, 766, 97
Offner, S. S. R., & Arce, H. G. 2015, ApJ, 811, 146
Offner, S. S. R., Klein, R. I., McKee, C. F., & Krumholz, M. R. 2009, ApJ, 703, 131
Olivier, G. M., Lopez, L. A., Rosen, A. L., et al. 2021, ApJ, 908, 68
Padoan, P. 1999, ApJ, 526, 279
Palla, F., & Stahler, S. W. 1991, ApJ, 375, 288
Palla, F., & Stahler, S. W. 1992, ApJ, 392, 667
Pelletier, G., & Pudritz, R. E. 1992, ApJ, 394, 117
Pittard, J. M., Wareing, C. J., & Kupilas, M. M. 2021, MNRAS, 508, 1768
Rosen, A. L., & Krumholz, M. R. 2020, AJ, 160, 78
Rosen, A. L., Krumholz, M. R., McKee, C. F., & Klein, R. I. 2016, MNRAS, 463, 2553
Rosen, A. L., Krumholz, M. R., Oishi, J. S., Lee, A. T., & Klein, R. I. 2017, JCoPh, 330, 924
Rosen, A. L., Li, P. S., Zhang, Q., & Burkhart, B. 2019, ApJ, 887, 108

---

[9] Because she is a cat.

Rosen, A. L., Lopez, L. A., Krumholz, M. R., & Ramirez-Ruiz, E. 2014, MNRAS, 442, 2701

Rosen, A. L., Offner, S. S. R., Foley, M. M., & Lopez, L. A. 2021, arXiv:2107.12397

Rosen, A. L., Offner, S. S. R., Sadavoy, S. I., et al. 2020, SSRv, 216, 62

Seifried, D., Banerjee, R., Pudritz, R. E., & Klessen, R. S. 2012, MNRAS, 423, L40

Semenov, D., Henning, T., Helling, C., Ilgner, M., & Sedlmayr, E. 2003, A&A, 410, 611

Shestakov, A. I., & Offner, S. S. R. 2008, JCoPh, 227, 2154

Shu, F. H., Lizano, S., Ruden, S. P., & Najita, J. 1988, ApJL, 328, L19

Skinner, S. L., Sokal, K. R., & Güdel, M. 2019, ApJ, 871, 116

Smith, N. 2014, ARA&A, 52, 487

Stutz, A. M., & Gould, A. 2016, A&A, 590, A2

Sundqvist, J. O., Owocki, S. P., & Puls, J. 2018, A&A, 611, A17

Takagi, S.-i., Murakami, H., & Koyama, K. 2002, ApJ, 573, 275

Tan, J. C., Beltrán, M. T., Caselli, P., et al. 2014, Protostars and Planets VI, 149 (Tucson, AZ: University of Arizona Press)

Toala, J. A., & Arthur, S. J. 2018, MNRAS, 478, 1218

Townsley, L. K., Broos, P. S., Chu, Y.-H., et al. 2011, ApJS, 194, 16

Truelove, J. K., Klein, R. I., McKee, C. F., et al. 1997, ApJL, 489, L179

Truelove, J. K., Klein, R. I., McKee, C. F., et al. 1998, ApJ, 495, 821

Tsujimoto, M., Hosokawa, T., Feigelson, E. D., Getman, K. V., & Broos, P. S. 2006, ApJ, 653, 409

Turk, M. J., Smith, B. D., Oishi, J. S., et al. 2011, ApJS, 192, 9

Vink, J. S. 2018, A&A, 615, A119

Vink, J. S., de Koter, A., & Lamers, H. J. G. L. M. 2001, A&A, 369, 574

Weaver, R., McCray, R., Castor, J., Shapiro, P., & Moore, R. 1977, ApJ, 218, 377

Weingartner, J. C., & Draine, B. T. 2001, ApJ, 548, 296

Williams, G. M., Peretto, N., Avison, A., Duarte-Cabral, A., & Fuller, G. A. 2018, A&A, 613, A11

Yorke, H. W., & Sonnhalter, C. 2002, ApJ, 569, 846

Zhang, B., Reid, M. J., Menten, K. M., et al. 2013, ApJ, 775, 79

Zhang, Q., Wang, Y., Pillai, T., & Rathborne, J. 2009, ApJ, 696, 268

Zhao, B., Tomida, K., Hennebelle, P., et al. 2020, SSRv, 216, 43